

Dynamic flux surrogate-based partitioned methods for interface problems

Pavel Bochev^{1,*}, Justin Owen², Paul Kuberry¹

Abstract

Partitioned methods for coupled problems rely on data transfers between subdomains to synchronize the subdomain equations and enable their independent solution. By treating each subproblem as a separate entity, these methods enable code reuse, increase concurrency and provide a convenient framework for plug-and-play multiphysics simulations. However, accuracy and stability of partitioned methods depends critically on the type of information exchanged between the subproblems. The exchange mechanisms can vary from minimally intrusive remap across interfaces to more accurate but also more intrusive and expensive estimates of the necessary information based on monolithic formulations of the coupled system. These transfer mechanisms are separated by accuracy, performance and intrusiveness gaps that tend to limit the scope of the resulting partitioned methods to specific simulation scenarios. Data-driven system identification techniques provide an opportunity to close these gaps by enabling the construction of accurate, computationally efficient and minimally intrusive data transfer surrogates. This approach shifts the principal computational burden to an offline phase, leaving the application of the surrogate as the sole additional cost during the online simulation phase. In this paper we formulate and demonstrate such a *dynamic flux surrogate-based* partitioned method for a model advection-diffusion transmission problem by using Dynamic Mode Decomposition (DMD) to learn the dynamics of the interface flux from data. The accuracy of the resulting DMD flux surrogate is comparable to that of a dual Schur complement reconstruction, yet its application cost is significantly lower. Numerical results confirm the attractive properties of the new partitioned approach.

Keywords: partitioned scheme, dynamic mode decomposition (DMD), interface, transmission problem

1. Introduction

Broadly speaking, numerical solution of coupled multiphysics problems can be approached in two distinct ways [1]. *Monolithic methods* treat the coupled system as a single entity and advance all of its constituent physics components in time simultaneously [1]. Typically this is accomplished by forming and solving a well-posed monolithic problem in which the coupling conditions are enforced by, e.g., Lagrange multipliers, or by using shared basis functions that are continuous across the interface [2]. As a result, monolithic methods possess excellent stability and accuracy properties but tend to be more computationally expensive. In particular, their solution requires sophisticated, *physics-based* preconditioners [3] in conjunction with, e.g., Jacobian-free Newton-Krylov solvers [4]. In terms of software development and code reuse, these methods are also rather inflexible since their modification to include and/or exclude a particular constituent physics

*Corresponding author

Email addresses: pbboche@sandia.gov (Pavel Bochev), jowen@sandia.gov (Justin Owen), pakuber@sandia.gov (Paul Kuberry)

¹Center for Computing Research, Sandia National Laboratories, Albuquerque, NM 87185, USA

²Applied Information Sciences, Sandia National Laboratories, Albuquerque, NM 87185, USA

³This paper describes objective technical results and analysis. Any subjective views or opinions that might be expressed in the paper do not necessarily represent the views of the U.S. Department of Energy or the United States Government. Sandia National Laboratories is a multimission laboratory managed and operated by National Technology and Engineering Solutions of Sandia, LLC., a wholly owned subsidiary of Honeywell International, Inc., for the U.S. Department of Energy's National Nuclear Security Administration under contract DE-NA-0003525. SAND2024-012150

component is a non-trivial task that may require significant code refactoring up to reimplementation from scratch.

In contrast, *partitioned methods* treat the subproblems comprising the multi-physics system as separate entities and advance them in time independently from each other [1]. Interactions between the subproblems and their synchronization is performed via data transfers over coupling windows; see, e.g., [5] for a representative example. This independent treatment of each constituent physics component makes partitioned schemes inherently more flexible than their monolithic counterparts. In particular, they enable code reuse, increase concurrency and improve simulation efficiency by allowing one to utilize codes optimized for the individual characteristics of each subproblem. As a result, partitioned schemes provide a convenient framework for plug-and-play multi-physics simulation capabilities, which are desirable in applications such as, e.g., earth system modeling.

The flexibility of partitioned schemes also means that their taxonomy is more fluid⁴ and depends on how one decides to “slice the pie.” In this paper we shall classify partitioned methods based on the “quality” of the spatial field information being exchanged between the subproblems, because it is one of the key factors governing the stability and the accuracy properties of this class of methods.

One of the most straightforward and computationally efficient exchange mechanisms for a partitioned method is solution remap across interfaces, followed by insertion of the remapped solution data into the appropriate coupling condition to “close” the subdomain equations and enable their independent solution. We refer to methods utilizing this *transfer-estimate-solve* mechanism as *remap-based* partitioned methods. Remap can be performed by using common refinement grids [6], linear maps [7], or meshless techniques; see [8, 9, 10, 11]. A detailed comparison of several popular mesh-based and mesh-free remap techniques can be found in [12].

The relatively low computational cost of remap and its minimally intrusive nature are two of the key reasons that remap-based partitioned schemes are often the default algorithmic choice for the large-scale solution of complex multi-physics problems ranging from Earth System Models (ESM) [13, 14] to nuclear power generation [15, 16]. For example, most ESMs utilize remap-based partitioned solvers built on a “hub-and-spoke” architecture where a “flux coupler” [17] at the hub coordinates the data transfers between the ESM components (land, ocean, atmosphere, sea-ice, and etc.) at the end of each spoke.

Mathematically, remap-based partitioned methods are equivalent to a single step of an iterative solution scheme such as fixed point iteration, preconditioned Richardson iteration, or an alternating Schwarz method [18, 19, 16, 20]. The iterative basis of remap-based partitioned methods is also their greatest liability, because a single iteration may not be enough to ensure sufficient stability and accuracy of the partitioned solution. Also, in certain cases, allowing more iterations can lead to divergence, e.g, the added mass instability [21]. Common mitigation strategies include Anderson acceleration [22], optimized Robin-like transmission conditions [23, 24, 20], optimized Schwarz methods [25, 26, 27], or simply performing enough iterations to ensure acceptable convergence of the partitioned solution.

A more robust alternative to remap-based partitioned methods can be developed by starting from a well-posed monolithic formulation of the coupled problem of the kind one would use to develop a monolithic solution method. However, instead of solving this monolithic system as a single entity, one uses techniques such as static condensation and/or Schur complements to recover highly accurate approximations of the interface fluxes. These fluxes provide boundary conditions that “close” the equations for the constituent physics components and enable their independent advancement in time. Conceptually, the difference between estimating the flux from remapped interface data and recovering it from the subdomain states is similar to the difference between computing a flux directly from the finite element solution vs. reconstructing this quantity by solving a variational problem [28]. Accordingly we shall refer to partitioned methods that recover accurate interface flux approximations from the states as *reconstruction-based*.

A few representative examples of reconstruction-based partitioned methods include the classical FETI approach [29], the localized Lagrange multiplier methods [30, 31, 32, 33], the displacement-based partitioned

⁴For example, time integration alone provides several classification options such as synchronous vs. asynchronous, multi-rate vs. single rate, and homogeneous vs. heterogeneous.

approach [34], the Implicit Value Recovery (IVR) method [35] and the Interface Flux Recovery (IFR) scheme [36]. Reconstruction-based partitioned methods can also be combined with the idea of Heterogeneous Asynchronous Time Integration [37, 38] to obtain Partitioned Heterogeneous Time Integration (PHTI) schemes [39].

All of the methods cited above start from a well-posed monolithic formulation of the coupled problem. Where these methods differ is in the type of the monolithic problem and in the manner in which they represent and reconstruct the interface flux. For example, localized Lagrange multiplier methods are based on a three-field monolithic formulation [40] in which the coupling conditions are enforced at the interface nodes, resulting in simple Boolean constraint matrices. The nodal values of the multipliers are then determined by a least-squares procedure. In contrast, FETI and IVR methods typically use two-field formulations, standard nodal finite elements for the Lagrange multiplier, and the dual Schur complement of the monolithic problem to estimate the interface flux. Finally, IFR is an example of a reconstruction-based partitioned method that does not use Lagrange multipliers to define the underlying monolithic problem. This scheme is designed for the non-standard *bulk coupling condition* [41] and the monolithic problem is constructed by treating the interface flux and the bulk condition as a new dependent variable and a new equation, respectively. The interface flux is represented by nodal elements and estimated by solving a dual Schur complement-like problem similar to the one in the IVR and FETI schemes.

At the same time, the accuracy and stability improvements afforded by the more precise flux estimates in reconstruction-based partitioned methods come at the cost of additional storage and computational burdens required to form and solve the linear system for the reconstruction of the flux. In some cases, such as when IVR [35] and IFR [36] utilize lumped mass matrices, these costs are moderate because the dual Schur complement is a sparse matrix dimensioned by the number of interface nodes. However, realization of the full accuracy potential of these methods requires consistent subdomain mass matrices. Inversion of these matrices results in a dense Schur complement with increased storage requirements, while forming the right hand sides of the associated linear systems for the interface flux adds a non-negligible computational cost to the exchange step. Since these operations also require access to the discretized subdomain equations, reconstruction-based partitioned methods tend to be more intrusive than remap-based schemes.

In a nutshell, the difference between the type of information exchanged in remap-based and reconstruction-based partitioned methods creates an accuracy, performance and intrusiveness gaps that tend to limit the application of each type of method to a relatively narrow simulation context.

Data-driven system identification techniques provide an opportunity to close these gaps by enabling the construction of accurate, computationally efficient and minimally intrusive surrogates for the dynamics of the interface flux. This approach shifts the principal computational burden to an *offline* phase, leaving the application of the surrogate as the sole additional cost during the *online* simulation phase. Typically, this cost amounts to just a few matrix-vector multiplications and is comparable to the cost of, e.g., remap via linear maps [7]. Furthermore, learning the surrogate does not require access to the discretized equations, which makes it minimally intrusive. Last but not least, with carefully designed training sets, the surrogate models can produce flux approximations whose accuracy is comparable to those obtained by, e.g., solution of the dual Schur complements.

We term this new class of schemes *dynamic flux surrogate-based* partitioned methods. Algorithmically, formulation of such a partitioned scheme requires two principal ingredients:

- a time stepping harness comprising a set of synchronization points in time and a choice of time integration schemes for each subproblem;
- a model form for performing system identification of the dynamic flux surrogate.

A dynamic flux surrogate-based partitioned method is not necessarily a general purpose solver intended to simulate a given coupled system for arbitrary choices of its inputs. Instead, this approach targets *parameterized* problems in which the states of the system are assumed to have a relatively “nice” dependence on a finite dimensional parameter vector $\boldsymbol{\mu} \in \mathbb{R}^m$. Thus, in this paper we develop and demonstrate dynamic flux surrogate-based partitioned methods for coupled parameterized Partial Differential Equations (μ PDEs).

Since our main goal is to provide an initial demonstration for this class of partitioned methods, we shall restrict attention to a simple, explicit, synchronous time stepping framework in which all subproblems are advanced in time using identical time steps and the same explicit time integrator. Likewise, as a model form for the flux surrogate, we choose a simple linear discrete time dynamical system and specialize the classical dynamic mode decomposition (DMD) [42, 43] to identify this model.

We first consider the case of a coupled μ PDE problem with a fixed parameter value and show that, with proper training data, a DMD flux surrogate (DMD-FS) can be constructed offline to accurately represent the dynamics of the interface flux for initial conditions not included in the training data. We then extend the DMD-FS to the parametric setting and develop a parametric DMD-FS (μ DMD-FS) to predict the flux for coupled μ PDEs. We show that μ DMD-FS can handle both parameters and initial conditions outside the training data. We then use the DMD flux surrogates to formulate and demonstrate numerically an instance of an explicit synchronous dynamic flux surrogate-based partitioned scheme for our coupled μ PDE problem.

To the best of our knowledge, this work is the first to consider dynamic interface surrogates as a way to improve the accuracy and efficiency of partitioned schemes. While other efforts in this direction exists, they have focussed primarily on improving the efficiency of the alternating Schwarz method for multiphysics problems by developing *static* surrogates for the Poincaré-Steklov operators that give the boundary response of the subdomain problems.

For example, [44] considers a “single simulation” scenario in which only one component of a coupled system has to be approximated accurately. To perform such simulations efficiently via Schwarz, the Poincaré-Steklov operators expressing the interactions between the subdomain of interest and the remaining subdomains are replaced by low-rank approximations of the Neumann-to-Dirichlet maps based on the first few eigenfunctions of the Laplace-Beltrami operators on the interfaces. Similarly, [45] develops an accelerated Schwarz framework for solving multiscale PDEs by training a neural network surrogate for the Dirichlet-to-Dirichlet map between the subdomains. As a final example, we mention [46] which considers a non-overlapping Schwarz iteration to solve coupled multiphysics problems. The fixed-point iteration is first expressed in terms of two Poincaré-Steklov operators realizing the Dirichlet-to-Neumann and the Neumann-to-Dirichlet maps. Then, each one of these maps is replaced by a surrogate based on kernel interpolation or neural net regression.

The rest of this article is organized as follows. Section 2 introduces the relevant notation and technical background. For the convenience of the reader, in Section 2.2, we also review the classic DMD approach [42] and a version of parametric DMD known as reduced Koopman operator interpolation (rKOI) [47].

Section 3 describes the coupled μ PDE model problem and defines the explicit synchronous time stepping framework for its partitioned solution. For completeness, we include example instantiations of this framework corresponding to a generic remap-based scheme and the IVR reconstruction-based partitioned scheme [35]. The section concludes with two algorithms describing two different implementations of the IVR scheme that will serve as benchmarks for the subsequent evaluation of the dynamic flux surrogate-based method. Sections 4–5 are the core of this paper, where we develop the DMD flux surrogates for the interface flux dynamics and formulate the training approach for their identification. Section 6 illustrates numerically the performance of the new μ DMD-FS partitioned scheme by comparing its accuracy and efficiency with the benchmark schemes described in Section 3. Section 7 summarizes our findings, outlines future research directions and offers some conclusions.

2. Notation and background

Section 2.1 below summarizes the notation that will be used throughout the paper. Section 2.2 reviews the original Dynamic Mode Decomposition (DMD) method, while Section 2.2.1 summarizes its parametric version.

2.1. Notation

Let $\Omega \in \mathbb{R}^\nu$, $\nu = 2, 3$ be a bounded region with Lipschitz continuous boundary Γ . We assume that Ω is divided into two non-overlapping subdomains Ω_1 and Ω_2 by an interface γ , as shown in Figure 1. This

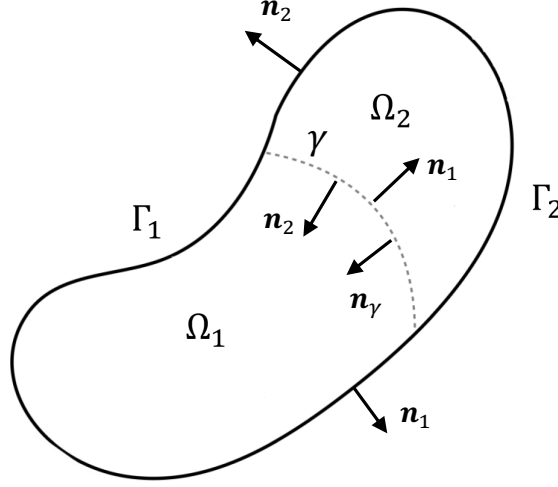


Figure 1: A two-dimensional domain Ω partitioned into two non-overlapping subdomains, Ω_1 and Ω_2 , with interface γ .

configuration is sufficient for our purposes, however the techniques developed in this paper can be easily extended to interface problems with more than two subdomains. We orient the interface by its unit normal \mathbf{n}_γ . Without a loss of generality we assume that \mathbf{n}_γ points towards Ω_1 and set $\Gamma_i := \partial\Omega_i \setminus \gamma$, $i = 1, 2$. We denote the unit outer normal to $\partial\Omega_i$ as \mathbf{n}_i . Note that \mathbf{n}_2 coincides with \mathbf{n}_γ along the interface.

In what follows $L^2(\Omega_i)$ will denote the space of all square integrable functions in Ω_i with norm and inner product denoted by $\|\cdot\|_{0,\Omega_i}$ and $(\cdot, \cdot)_{0,\Omega_i}$, respectively. Similarly, $H^1(\Omega_i)$ is the Sobolev space of order one on Ω_i with norm $\|\cdot\|_{1,\Omega_i}$ and $H_D^1(\Omega_i)$ will denote the subspace of $H^1(\Omega_i)$ whose elements vanish on Γ_i . We will also need the trace space $H^{1/2}(\gamma)$, with dual $H^{-1/2}(\gamma)$ and duality pairing $\langle \cdot, \cdot \rangle_\gamma$.

The symbol Ω_i^h will stand for a conforming quasi-uniform [48] partition of Ω_i into finite elements $K_{i,s}$ with vertices $\mathbf{x}_{i,r}$ and mesh parameter h_i . We denote the total number of nodes in Ω_i^h by n_i . Each Ω_i^h induces a conforming mesh Γ_i^h on the Dirichlet boundary Γ_i with $n_{i,\Gamma}$ nodes. In this paper we shall assume that Ω_1 and Ω_2 are meshed independently. As a result, their finite element partitions Ω_1^h and Ω_2^h induce two independent finite element meshes on the interface γ denoted by γ_1^h and γ_2^h , respectively, with $n_{i,\gamma}$ nodes each. For simplicity we restrict attention to spatially coincident discrete interfaces, however, the nodes on γ_1^h and γ_2^h are not required to match.

For the purposes of this work it suffices to consider standard nodal C^0 finite element spaces S_i^h defined with respect to Ω_i^h . We recall that S_i^h is a conforming subspace of $H^1(\Omega_i)$; see, e.g., [48]. The elements of S_i^h that vanish on the Dirichlet boundary Γ_i form the subspace $S_{i,D}^h$, which is a conforming approximation of $H_D^1(\Omega_i)$. Restriction of S_i^h to Γ_i and γ induce the boundary space $S_{i,\Gamma}^h$ and the interface space $S_{i,\gamma}^h$, respectively. We endow S_i^h with a standard Lagrangian basis $\{\ell_{i,r}\}$ such that $\ell_{i,r}(\mathbf{x}_{i,s}) = \delta_{rs}$, where δ_{rs} is the Kronecker δ -symbol.

Dimensions of lowest-order C^0 finite element spaces considered in this paper equal the number of free nodes in their respective finite element partitions. Thus, $\dim S_i^h = n_i$, $\dim S_{i,D}^h = n_{i,D} := n_i - n_{i,\Gamma}$, $\dim S_{i,\Gamma}^h = n_{i,\Gamma}$, and $\dim S_{i,\gamma}^h = n_{i,\gamma}$. Let $\mathbf{u}_i \in \mathbb{R}^{n_i}$ denote the coefficient vector of the finite element function $u_i^h \in S_i^h$. Without a loss of generality we shall assume that the nodes of Ω_i^h are numbered in such a way that \mathbf{u}_i is partitioned as $\mathbf{u}_i = (\mathbf{u}_{i,\gamma}, \mathbf{u}_{i,0}, \mathbf{u}_{i,\Gamma})$, where $\mathbf{u}_{i,\gamma} \in \mathbb{R}^{n_{i,\gamma}}$, $\mathbf{u}_{i,0} \in \mathbb{R}^{n_{i,0}}$, and $\mathbf{u}_{i,\Gamma} \in \mathbb{R}^{n_{i,\Gamma}}$ are vectors corresponding to the interface, interior, and Dirichlet coefficients of u_i^h , respectively. Note that with this convention the coefficient vector of $u_{i,D}^h \in S_{i,D}^h$ can be partitioned as $\mathbf{u}_{i,D} = (\mathbf{u}_{i,\gamma}, \mathbf{u}_{i,0}, \mathbf{0})$.

2.2. Dynamic Mode Decomposition

Dynamic Mode Decomposition (DMD) [42, 43] is a data driven algorithm that infers an approximation for the flow map of a dynamical system from snapshots $\mathbf{y}(t)$ of its solutions. Specifically, given s equally

spaced in time solution snapshots $\mathbf{y}_i := \mathbf{y}(t_i)$ DMD seeks an operator A such that

$$\mathbf{y}_{i+1} \approx A\mathbf{y}_i. \quad (1)$$

To approximate the discrete flow map A we arrange the snapshots into matrices $\mathbf{Y} := [\mathbf{y}_i]_{i=0}^{s-1}$ and $\mathbf{Y}' := [\mathbf{y}_i]_{i=1}^s$. Then, equation (1) implies the relationship

$$\mathbf{Y}' \approx A\mathbf{Y}. \quad (2)$$

DMD treats (2) as a linear system for the unknown operator A . “Solving” this linear system yields $A = \mathbf{Y}'\mathbf{Y}^+$ where \mathbf{Y}^+ is the Moore-Penrose pseudo-inverse. An effective way to estimate the pseudo-inverse is provided by its truncated singular value decomposition (SVD). To that end, one computes the SVD $Y = U\Sigma V^T$ of the snapshot matrix and retains the first k left singular vectors (“modes”) corresponding to the k leading singular values. This yields the approximation

$$\mathbf{Y}^+ = V\Sigma^+U^T \approx V_k\Sigma_k^+U_k^T =: \mathbf{Y}_k^+, \quad (3)$$

where V_k , Σ_k^+ , and U_k are the truncated SVD matrices. Using \mathbf{Y}_k^+ in lieu of \mathbf{Y}^+ then results in the following DMD approximation of the flow map:

$$A \approx A_k := \mathbf{Y}'\mathbf{Y}_k^+ = \mathbf{Y}'V_k\Sigma_k^+U_k^T. \quad (4)$$

We refer to A_k as the DMD operator. The accuracy of the DMD operator depends on the number k of modes retained in the truncated SVD approximation of the snapshot matrix Y . This number is usually selected to be the minimum positive integer for which

$$1 - E_k(Y) \leq \epsilon, \quad (5)$$

where $0 < \epsilon < 1$ is a given tolerance and

$$E_k(Y) := \frac{\sum_{i=1}^k \sigma_i^2}{\sum_{i=1}^n \sigma_i^2}. \quad (6)$$

In (6) σ_i is the i^{th} singular value of Y , n is the total number of singular values, and $E_k(Y)$ is the relative snapshot energy captured by the first k modes. Algorithm 1 summarizes the computation of the DMD operator

Algorithm 1: DMD Algorithm

1. Simulate the dynamical system of interest to generate a collection of s , equally spaced in time, solution snapshots \mathbf{y}_i and arrange them into matrices \mathbf{Y} and \mathbf{Y}' .
 2. Compute the SVD $\mathbf{Y} = U\Sigma V^T$ of the snapshot matrix.
 3. Select a tolerance $0 < \epsilon < 1$ and find the smallest positive integer k for which (5) holds.
 4. Retain the first k left singular vectors and compute the approximate pseudo-inverse \mathbf{Y}_k^+ as in (3).
 5. Compute the DMD operator A_k as in (4).
-

Remark 1. In typical modeling situations the DMD operator is applied repeatedly to a given initial state y_0 to simulate the evolution of a dynamical system over a sequence of time steps t_1, t_2, \dots, t_n . In this case simulation efficiency can be significantly improved by replacing A_k with a reduced order DMD operator $\tilde{A}_k := U_k^T A_k U_k \in \mathbb{R}^{k \times k}$ which acts on a reduced state $\tilde{y}_i = U_k^T y_i$. In contrast, here we shall always use the DMD operator over a single time interval to predict the full order interface flux at the future time from the full order flux at the current time. In this context, switching to a reduced order operator \tilde{A}_k is not justified because the cost of projecting a full state onto a reduced state and back to a full state cannot be amortized over a single time step.

2.2.1. Parametric Dynamic Mode Decomposition

In the context of dynamical systems corresponding to parameterized PDEs (μ PDEs), the standard DMD Algorithm 1 can provide accurate approximation of the flow map only for given fixed set of parameters $\boldsymbol{\mu}$. Development of the dynamic flux surrogate-based partitioned method for coupled μ PDEs requires extension of the DMD approach to the parametric context. There are several approaches that can be used to accomplish this, however they all involve sampling of the parameter space $\mathcal{M} \subset \mathbb{R}^M$ to define a representative set of parameter values $\mathcal{M}_m := \{\boldsymbol{\mu}_i\}_{i=1}^m$. One then simulates the dynamical system of interest for all parameters in this set to generate a collection of parameterized snapshot matrices $\mathbf{Y}(\boldsymbol{\mu}_i)$ and $\mathbf{Y}'(\boldsymbol{\mu}_i)$; for all $\boldsymbol{\mu}_i \in \mathcal{M}_m$.

The stacked DMD technique [49] assumes that the states for all parameter values were sampled at the same time instances. This allows one to “stack” the snapshots $\mathbf{Y}(\boldsymbol{\mu}_i)$ and $\mathbf{Y}'(\boldsymbol{\mu}_i)$ into composite snapshot matrices $[\mathbf{Y}(\boldsymbol{\mu}_i)]_{i=1}^m$ and $[\mathbf{Y}'(\boldsymbol{\mu}_i)]_{i=1}^m$ containing the known state data for all $\boldsymbol{\mu}_i \in \mathcal{M}_m$. Then, one applies the standard DMD algorithm (Algorithm 1) to the composite snapshot matrices. The estimated state for a new parameter value $\boldsymbol{\mu} \notin \mathcal{M}_m$ is then computed by interpolating between the output state values. One possible drawback of the stacked DMD technique is that all possible parameter values, including those far from the current parameter value of interest, contribute to the singular value decomposition of the composite snapshot matrix $[\mathbf{Y}(\boldsymbol{\mu}_i)]_{i=1}^m$.

Reduced Koopman operator inference (rKOI) was introduced in [47] as a parametric approach to DMD that localizes the interpolation process. Given a new parameter value $\boldsymbol{\mu} \notin \mathcal{M}_m$ this approach starts by choosing a ball $B(\boldsymbol{\mu}, r) \subset \mathcal{M}$ of radius r , centered at $\boldsymbol{\mu}$. Then, rKOI uses Algorithm 1 to compute the DMD operators $A_{k_j}(\boldsymbol{\mu}_j)$ for all

$$\boldsymbol{\mu}_j \in \mathcal{M}_m(\boldsymbol{\mu}, r) := \mathcal{M}_m \cap B(\boldsymbol{\mu}, r). \quad (7)$$

A Lagrange interpolant is then constructed from the set of DMD operators $\{A_{k_j}(\boldsymbol{\mu}_j) \mid \boldsymbol{\mu}_j \in \mathcal{M}_m(\boldsymbol{\mu}, r)\}$ and queried at $\boldsymbol{\mu}$ to produce $A(\boldsymbol{\mu})$. Unlike the stacked DMD approach, rKOI creates a DMD operator for each parameter $\boldsymbol{\mu}_i \in \mathcal{M}_m$, and only operators corresponding to parameters close to the parameter of interest $\boldsymbol{\mu}$ contribute to the approximation of the flow map at the latter.

3. Model problem and a partitioned framework for its solution

To develop and demonstrate the dynamic flux surrogate-based partitioned method, we consider a scalar advection-diffusion transmission problem parameterized by the diffusion coefficient in each subdomain. This problem, its sub-problems and the relevant weak formulations are presented in Section 3.1. Section 3.2 defines a framework for the partitioned solution of the model problem, built on a simple explicit synchronous time stepping harness, and provides examples of a remap-based and reconstruction-based instantiation of this framework.

3.1. Model Transmission Problem

The transmission problem considered in this paper comprises a pair of subdomain μ PDEs

$$\begin{cases} \dot{u}_i - \nabla \cdot F_i(u_i) = f_i & \text{in } \Omega_i \times [0, T] \\ u_i = g_i & \text{in } \Gamma_i \times [0, T] \\ u_i(\mathbf{x}, 0) = u_{i,0}(\mathbf{x}) & \text{in } \Omega_i \end{cases} \quad i = 1, 2, \quad (8)$$

coupled by using standard interface compatibility conditions

$$u_1(\mathbf{x}, t) = u_2(\mathbf{x}, t) \quad \text{and} \quad F_1(u_1) \cdot \mathbf{n}_\gamma = F_2(u_2) \cdot \mathbf{n}_\gamma \quad \text{on } \gamma \times [0, T], \quad (9)$$

that enforce continuity of the states and the fluxes on the interface, respectively. In (8)–(9), f_i , g_i and $u_{i,0}$ are a given source term, Dirichlet boundary data, and initial condition, respectively,

$$F_i(u_i) = \kappa_i \nabla u_i - \mathbf{v} u_i, \quad i = 1, 2;$$

is the total flux, $\kappa_i > 0$ is the diffusion coefficient in Ω_i and \mathbf{v} is a velocity field. We assume that each subdomain problem is parameterized by its respective diffusion coefficient κ_i .

The problem (8)–(9) models the diffusive transport of a scalar quantity across an interface separating two different materials. In this setting γ is a physical interface that corresponds to a jump in a material property such as diffusivity, permittivity, or thermal conductivity. This type of problems is often referred to as “transmission” problems (TP).

Remark 2. *The surrogate-based partitioned approach formulated in this paper is agnostic to the interface type and can be applied both to problems such as (8)–(9), where the interface is physical, and to problems where the interface is introduced to increase, e.g., the parallel efficiency. Similarly, although here we only consider the standard coupling conditions (9), the approach can be easily extended to nonstandard coupling conditions such as the bulk condition [41].*

3.1.1. Subdomain problems closure

Considered as a standalone PDE on Ω_i , each subdomain equation in (8) is incomplete in the sense that it lacks boundary data on the part of $\partial\Omega_i$ that coincides with the interface γ . To close the subdomain PDEs one can specify Dirichlet, Neumann or Robin-type boundary conditions. The first two cases often appear in the context of non-overlapping alternating Schwarz methods [18, 19], while the third case is characteristic of optimized transmission conditions for Schwarz domain decomposition [50, 26, 20] and fluid-structure interaction [23, 51]. The second case, i.e., closure by Neumann boundary conditions, is also commonly encountered in methods originating in monolithic formulations based on Lagrange multipliers.

Although the dynamic flux surrogate-based partitioned approach can be developed with surrogates for either one of the above three options, we chose to work with the second one and treat γ as a Neumann boundary. The primary reason for this choice is that it will enable us to compare the accuracy of our surrogate flux with the “gold” standard in which the flux is computed by solving the dual Schur complement of a mixed monolithic formulation of the transmission problem (8)–(9). Letting $\lambda = F_1(u_1) \cdot \mathbf{n}_\gamma = F_2(u_2) \cdot \mathbf{n}_\gamma$ be the unknown flux across the interface and treating λ as Neumann boundary data, we obtain the following, formally complete versions of the subdomain equations:

$$\left\{ \begin{array}{ll} \dot{u}_i - \nabla \cdot F_i(u_i) = f_i & \text{in } \Omega_i \times (0, T] \\ u_i = g_i & \text{on } \Gamma_i \times (0, T] \\ F_i(u_i) \cdot \mathbf{n}_i = (-1)^i \lambda & \text{on } \gamma \times (0, T] \\ u_i(\mathbf{x}, 0) = u_{i,0}(\mathbf{x}) & \text{in } \Omega_i \end{array} \right. ; \quad i = 1, 2. \quad (10)$$

The subdomain PDEs (10) are mixed boundary value problems that can be solved independently from each other one as long as λ or an approximation of λ is known. In the next section we will formulate a simple framework for the partitioned solution of (8)–(9) that builds on this observation. We will state this framework using a standard nodal Galerkin semi-discretizations of (10) in space, however, the approach is generic enough and applicable to a wide range of spatial discretizations.

To that end, let us recall the weak variational formulations of the subdomain PDEs (10) that underpin their Galerkin discretization. Assume that $f_i(\cdot, t) \in H^{-1}(\Omega_i)$, $g_i(\cdot, t) \in H_{00}^{1/2}(\Gamma_i)$, $\lambda(\cdot, t) \in H^{-1/2}(\gamma)$; $t \in (0, T]$, and $u_{i,0} \in H^1(\Omega_i)$ are given. Then, for $i = 1, 2$ and all $0 < t \leq T$ we seek $u_i(\cdot, t) \in H^1(\Omega_i)$ satisfying the initial condition, the Dirichlet boundary condition, and such that there holds

$$(\dot{u}_i, v_i)_{0,\Omega_i} + (F_i(u_i), \nabla v_i)_{0,\Omega_i} = (f_i, v_i)_{0,\Omega_i} + (-1)^i \langle \lambda, v_i \rangle_\gamma \quad \forall v_i \in H_D^1(\Omega_i). \quad (11)$$

Restriction of (11) to conforming finite element spaces $S_i^h \subset H^1(\Omega_i)$ and $S_{i,D}^h \subset H_D^1(\Omega_i)$, $i = 1, 2$ yields the semi-discrete in space Galerkin formulation of (10): seek $u^h(\cdot, t) \in S_i^h$ satisfying appropriate discrete versions of the initial and boundary conditions, such that for all $0 < t \leq T$ there holds

$$(\dot{u}_i^h, v_i^h)_{0,\Omega_i} + (F_i(u_i^h), \nabla v_i^h)_{0,\Omega_i} = (f_i, v_i^h)_{0,\Omega_i} + (-1)^i \langle \lambda, v_i^h \rangle_\gamma \quad \forall v_i^h \in S_{i,D}^h. \quad (12)$$

Without a loss of generality we shall assume that the Dirichlet boundary condition is imposed by using the interpolant of the boundary data, i.e., we seek the finite element solution as a sum $u_i^h = u_{i,D}^h + g_i^h$, where $u_{i,D}^h \in S_{i,D}^h$ and $g_i^h \in S_{i,\Gamma}^h$ is a finite element function such that $g_i^h(\mathbf{x}_{i,r}) = g_i(\mathbf{x}_{i,r})$ for all vertices $\mathbf{x}_{i,r} \in \Gamma_i^h$. The initial condition for (12) can be defined either by interpolation or L^2 projection of the initial data, i.e., by solving

$$(u_{i,0}^h, v_i^h)_{0,\Omega_i} = (u_{i,0}, v_i^h)_{0,\Omega_i} \quad \forall v_i^h \in S_i^h. \quad (13)$$

It is straightforward to check that, for $i = 1, 2$, (12) is equivalent to the following system of Ordinary Differential Equations (ODEs):

$$M_i \dot{\mathbf{u}}_i + K_i \mathbf{u}_i = \mathbf{f}_i + (-1)^i \boldsymbol{\lambda}_i, \quad t \in (0, T] \quad \text{and} \quad \mathbf{u}_i(0) = \mathbf{u}_{i,0}, \quad (14)$$

for the unknown coefficient vector $\mathbf{u}_i(t)$ of the finite element solution u_i^h . In the above system M_i and K_i are subdomain mass and stiffness matrices, respectively, and \mathbf{f}_i , $\mathbf{u}_{i,0}$, and $\boldsymbol{\lambda}_i$ are the coefficients of the projections of the source term, the initial condition, and the Neumann data onto $S_{i,D}^h$ and $S_{i,\gamma}^h$, respectively.

3.2. An explicit synchronous partitioned framework

Let $0 = t_0 < t_1 < \dots < t_N = T$ denote a uniform partition of the simulation time interval $[0, T]$ with time step Δt , i.e., $t_{k+1} = t_k + \Delta t$, $k = 0, \dots, N-1$. To define the time stepping harness for our framework, we use the above partition of $[0, T]$ to discretize time on both subdomains, set the synchronization points to coincide with the time discretization points, and use the explicit forward Euler scheme to advance the subdomain solutions in time.

To state the explicit synchronous partitioned framework let $\mathbf{u}_{i,m}$ and $\boldsymbol{\lambda}_{i,m}$ denote the coefficient vectors of the subdomain state $u_i^h(\mathbf{x}, t_m)$ and the interface flux $\lambda(\mathbf{x}, t_m)$ for $0 \leq m \leq N$. Assume that $\mathbf{u}_{i,k}$ has been determined at the current time step t_k , $k \geq 1$ using a flux vector $\boldsymbol{\lambda}_{i,k-1}$ and that all previous state and flux coefficient vectors are available. The explicit synchronous partitioned method computes the solution coefficients $\mathbf{u}_{i,k+1}$ at the future time step according to the following algorithm:

Algorithm 2: Explicit synchronous partitioned framework

Assume a partition $0 = t_0 < t_1 < \dots < t_N = T$ of the simulation time interval and compute the initial condition vectors $\mathbf{u}_{i,0}$, $i = 1, 2$. For $i = 1, 2$ and $k = 0, 1, \dots, N-1$:

1. **Synchronize:** Compute approximations $\boldsymbol{\lambda}_{i,k}$ of the interface flux at the current time step.
2. **Step in time:** Use forward Euler to solve (14) with Neumann data $\boldsymbol{\lambda}_{i,k}$:

$$\mathbf{u}_{i,k+1} = \mathbf{u}_{i,k} + \Delta t M_i^{-1} (\mathbf{f}_{i,k} - K_i \mathbf{u}_{i,k} + (-1)^i \boldsymbol{\lambda}_{i,k}). \quad (15)$$

Abstractly, the first step of Algorithm 2 can be stated in terms of generic synchronization operators \mathcal{F}_i acting on subsets $\mathbf{U}_{i,\alpha_{i,k}}$ and $\boldsymbol{\Lambda}_{i,\beta_{i,k-1}}$ of the available state and flux coefficient vectors, selected by multi-indices $\alpha_{i,k}$ and $\beta_{i,k-1}$, respectively, i.e.,

$$\boldsymbol{\lambda}_{i,k} = \mathcal{F}_i(\boldsymbol{\Lambda}_{1,\beta_{1,k-1}}, \boldsymbol{\Lambda}_{2,\beta_{2,k-1}}; \mathbf{U}_{1,\alpha_{1,k}}, \mathbf{U}_{2,\alpha_{2,k}}), \quad i = 1, 2. \quad (16)$$

To illustrate the significance of the synchronization operators \mathcal{F}_i for the properties of the resulting schemes below, we sketch a remap-based and reconstruction-based instantiation of our partitioned framework corresponding to two different choices of these operators.

A remap-based method. Linear maps [7] define the data transfer between the subdomains as

$$\hat{\mathbf{u}}_1 = R_{2 \rightarrow 1} \mathbf{u}_2 \quad \text{and} \quad \hat{\mathbf{u}}_2 = R_{1 \rightarrow 2} \mathbf{u}_1,$$

where the hat accent denotes a remapped field and $R_{2 \rightarrow 1}$ and $R_{1 \rightarrow 2}$ are linear operators constructed to satisfy specific accuracy, consistency, conservation and monotonicity properties. These maps can be defined between different types of discretizations including finite volume, finite difference and finite elements, which makes them well-suited for models that employ a “zoo” of meshes and discretizations, such as DOE’s E3SM earth system model [14]. We note that definition of linear maps may require construction of additional overset or common refinement grids [6] on the interface. This is a fairly complex computational geometry task that can become expensive in three-dimensions.

Assume that the linear maps $R_{2 \rightarrow 1}$ and $R_{1 \rightarrow 2}$ have been constructed. We define the synchronization operators as

$$\mathcal{F}_1(\mathbf{u}_1, \mathbf{u}_2) := K_{1,\gamma} \hat{\mathbf{u}}_1 = K_{1,\gamma} R_{2 \rightarrow 1} \mathbf{u}_2 \quad \text{and} \quad \mathcal{F}_2(\mathbf{u}_1, \mathbf{u}_2) := K_{2,\gamma} \hat{\mathbf{u}}_2 = K_{2,\gamma} R_{1 \rightarrow 2} \mathbf{u}_1, \quad (17)$$

where $K_{i,\gamma}$ is an interface flux matrix, i.e., the algebraic form of the interface term

$$\langle F_i(u_i^h) \cdot \mathbf{n}_i, v^h \rangle_\gamma.$$

Utilization of the operators (17) at the synchronization stage of our partitioned framework yields an instance of a remap-based partitioned method that follows the “transfer-estimate-solve” procedure. The “transfer” part is performed by the linear maps, whereas the “estimate” part is accomplished by application of the interface flux matrix $K_{i,\gamma}$ to the remapped state.

Note that the latter step is equivalent to evaluation of the flux operator $F_i(\cdot)$ at the discrete remapped state. In the presence of diffusive flux components, i.e., when $\kappa_i > 0$, this operation involves differentiation of the discrete solution, which yields fluxes that are one order less accurate than the states. For the lowest-order C^0 spaces utilized in this paper, this means that the resulting partitioned solution will be only first-order accurate, even though the underlying finite element space is second-order accurate.

Remark 3. *The operators in (17) are used here only as an illustration for one of the many possible realizations of remap-based information exchange between the subdomains. For example, by reversing the order of the linear map and the interface flux matrix one obtains an operator $\mathcal{F}_i(\mathbf{u}_1, \mathbf{u}_2) = R_{j \rightarrow i} K_{j,\gamma} \mathbf{u}_j$ which remaps the flux instead of the state. The synchronization operators may also have different outputs providing a Neumann condition on one side of the interface and a Dirichlet condition on the other side, as is the case with fluid-structure interaction problems; see, e.g., [52].*

A reconstruction-based method. The basis for the accurate estimation of the interface flux in reconstruction-based partitioned schemes is typically provided by a well-posed monolithic formulation of the coupled problem (8)–(9). To define such a formulation we follow [35] and differentiate the first constraint in (9) in time to obtain the equivalent constraint

$$\dot{u}_1(\mathbf{x}, t) = \dot{u}_2(\mathbf{x}, t) \quad \text{on} \quad \gamma \times [0, T]. \quad (18)$$

Using a Lagrange multiplier $\lambda(\cdot, t) \in H^{-1/2}(\gamma)$ to enforce (18) yields the following weak monolithic formulation of the coupled problem (8)–(9): seek $\{u_1(\cdot, t), u_2(\cdot, t), \lambda(\cdot, t)\} \in H^1(\Omega_1) \times H^1(\Omega_2) \times H^{-1/2}(\gamma)$ satisfying the initial conditions, the Dirichlet boundary conditions, and such that for all $0 < t \leq T$ there holds

$$\begin{aligned} (\dot{u}_1, v_1)_{0,\Omega_1} + (F_1(u_1), \nabla v_1)_{0,\Omega_1} + \langle \lambda, v_1 \rangle_\gamma &= (f_1, v_1)_{0,\Omega_1} & \forall v_1 \in H_D^1(\Omega_1) \\ (\dot{u}_2, v_2)_{0,\Omega_2} + (F_2(u_2), \nabla v_2)_{0,\Omega_2} - \langle \lambda, v_2 \rangle_\gamma &= (f_2, v_2)_{0,\Omega_2} & \forall v_2 \in H_D^1(\Omega_2) \\ \langle u_1 - u_2, \mu \rangle_\gamma &= 0 & \forall \mu \in H^{-1/2}(\gamma) \end{aligned} \quad (19)$$

Restriction of (19) to conforming finite element subspaces for the states and the Lagrange multiplier yields the semi-discrete in space monolithic problem. It is straightforward to check that the latter is equivalent to a system of differential algebraic equations (DAEs)

$$\begin{aligned} M_1 \dot{\mathbf{u}}_1 + K_1 \mathbf{u}_1 + G_1^T \boldsymbol{\lambda} &= \mathbf{f}_1 \\ M_2 \dot{\mathbf{u}}_2 + K_2 \mathbf{u}_2 - G_2^T \boldsymbol{\lambda} &= \mathbf{f}_2 \\ G_1 \dot{\mathbf{u}}_1 - G_2 \dot{\mathbf{u}}_2 &= 0 \end{aligned} \quad (20)$$

Algorithm 3: Reconstruction-based IVR partitioned scheme

Offline

Let M_i , $i = 1, 2$ be the lumped mass matrix for IVR(L) or the consistent mass matrix for IVR(C).

1. Compute the Schur complement and its Cholesky factorization: $S = LL^T$.
2. For $i = 1, 2$ compute the matrices $H_i := G_i M_i^{-1}$.

Online

Assume a partition $0 = t_0 < t_1 < \dots < t_N = T$ of the simulation time interval and compute the initial condition vectors $\mathbf{u}_{i,0}$, $i = 1, 2$. For $i = 1, 2$ and $k = 0, 1, \dots, N - 1$:

1. Synchronize:

- 1.1 Compute the load vectors $\mathbf{b}_{i,k} = \mathbf{f}_{i,k} - K_i \mathbf{u}_{i,k}$ and the right hand side $\mathbf{c}_k := H_1 \mathbf{b}_{1,k} - H_2 \mathbf{b}_{2,k}$ of the linear system (21).
- 1.2 Solve the Schur complement equation (21) for $\boldsymbol{\lambda}_k$ and compute $\boldsymbol{\lambda}_{i,k} := G_i^T \boldsymbol{\lambda}_k$.

2. Step in time: Use forward Euler to solve (14) with Neumann data $\boldsymbol{\lambda}_{i,k}$:

$$\mathbf{u}_{i,k+1} = \mathbf{u}_{i,k} + \Delta t M_i^{-1} (\mathbf{b}_{i,k} + (-1)^i \boldsymbol{\lambda}_{i,k}), \quad i = 1, 2. \quad (23)$$

for the coefficient vectors \mathbf{u}_1 , \mathbf{u}_2 and $\boldsymbol{\lambda}$ of the subdomain states and the Lagrange multiplier, respectively. The matrices G_i in (20) define the algebraic form of the constraint (18). It is easy to see that the coefficient vector $\boldsymbol{\lambda}$ of the Lagrange multiplier solves the linear system

$$S\boldsymbol{\lambda} = G_1 M_1^{-1} \mathbf{b}_1 - G_2 M_2^{-1} \mathbf{b}_2, \quad (21)$$

where $\mathbf{b}_i = \mathbf{f}_i - K_i \mathbf{u}_i$ and

$$S = G_1 M_1^{-1} G_1^T + G_2 M_2^{-1} G_2^T$$

is the dual Schur complement of the 3×3 block matrix on the left-hand-side in (20). One can show that if the Lagrange multiplier is approximated by either one of the interface spaces $S_{i,\gamma}^h$, the matrix S is symmetric and positive definite and its condition number is bounded by a constant; see [35]. Assuming this choice, i.e., that $\boldsymbol{\lambda}$ is approximated by $\boldsymbol{\lambda}^h \in S_{l,\gamma}^h$ where $l = 1$ or $l = 2$, let $\boldsymbol{\lambda}$ denote the unique solution of (21). We then define the synchronization operators (16) as follows:

$$\mathcal{F}_i(\mathbf{u}_1, \mathbf{u}_2) := G_i^T \boldsymbol{\lambda} = G_i^T (G_1 M_1^{-1} G_1^T + G_2 M_2^{-1} G_2^T)^{-1} (G_1 M_1^{-1} \mathbf{b}_1 - G_2 M_2^{-1} \mathbf{b}_2). \quad (22)$$

Inserting these definitions into the partitioned framework yields the reconstruction-based IVR scheme [35].

In contrast to the remap-based scheme utilizing (17), IVR is second order accurate, i.e., it retains the accuracy of the underlying finite element space. Moreover, for subdomain grids with matching interface nodes, the IVR solution coincides with the solution of (20) computed by the explicit Euler method. In particular, IVR recovers exactly globally linear solutions of the model problem.

However, the higher accuracy of the IVR scheme comes at the price of a more intrusive implementation, larger storage requirements and higher computational costs. For example, computation of (22) requires access to the discrete constraint operators G_i and the subdomain mass matrices M_i . In contrast, evaluation of (17) only involves entities defined on, or adjacent to, the interface grid. Access to the latter is a minimum requirement for a partitioned scheme and so if the matrices $K_{i,\gamma}$, $i = 1, 2$ are not available from the codes, they can be assembled by the coupler.

Similarly, while the Schur complement matrix S and the matrix products $G_i M_i^{-1}$ can be precomputed and factored, their storage requires additional⁵ $O(n_{l,\gamma}^2)$ and $O(n_{i,D} n_{l,\gamma})$ units of floating point storage, respectively. Finally, the cost of application of $G_i M_i^{-1}$ is proportional to the dimension of the subdomain problem rather than just its interface portion.

The cost of the IVR scheme can be reduced to roughly that of a remap-based method by switching to a lumped mass approximation of the consistent mass matrices. While the resulting scheme remains connected to the monolithic problem (19) and remains provably well-posed [35], its accuracy drops to first-order. Following [35] we term the consistent and lumped mass versions of IVR as IVR(C) and IVR(L), respectively. We will use IVR(C) and IVR(L) as benchmarks for the surrogate-based method. We refer to Algorithm 3 for a concise description of the IVR scheme.

3.2.1. Complexity analysis of the IVR scheme

The cost of IVR(C) in Algorithm 3 includes computation⁶ of the right hand side vector \mathbf{c}_k and solution of the Schur complement equation for $\boldsymbol{\lambda}_k$. Assume for simplicity that the meshes on both subdomains have the same numbers of interface and interior nodes, i.e., $n_{1,D} = n_{2,D}$ and $n_{1,\gamma} = n_{2,\gamma}$. Then, the cost of the first operation is $2n_{1,\gamma}(2n_{1,D} - 1)$ flops, whereas the second one takes $2n_{1,\gamma}^2$ flops. Since in general the number of interface DoFs $n_{1,\gamma}$ is much smaller than the number $n_{1,D}$ of interior DoFs, computation of \mathbf{c}_k dominates the cost of IVR(C).

The efficiency gains of the IVR(L) scheme stem from the fact that the lumped mass matrices have a block diagonal structure $M_i = \text{diag}(M_{i,\gamma}, M_{0,\gamma})$ where $M_{i,\gamma}$ and $M_{0,\gamma}$ are $n_{i,\gamma} \times n_{i,\gamma}$ and $n_{i,D} \times n_{i,D}$ diagonal matrices associated with the interface and interior degrees-of-freedom, respectively. As a result, in the lumped mass instance of the monolithic problem (20) underpinning IVR(L), the interface degrees of freedom are completely decoupled from the interior ones. In particular, computation of the right hand side vector \mathbf{c}_k , which dominates the cost of IVR(C), now reduces to

$$\mathbf{c}_k = H_{1,\gamma}(\mathbf{b}_{1,k})_\gamma - H_{2,\gamma}(\mathbf{b}_{2,k})_\gamma,$$

where $(\cdot)_\gamma$ denotes a sub-vector of coefficients indexed by the interface nodes and $H_{i,\gamma} = G_i M_{i,\gamma}^{-1}$ is $n_{1,\gamma} \times n_{i,\gamma}$. The cost of this operation is $2n_{1,\gamma}(2n_{1,\gamma} - 1) \approx O(n_{1,\gamma}^2)$. Since the cost of the Schur complement solve is unchanged, it follows that the total cost of IVR(L) is $O(n_{1,\gamma}^2)$ whereas the total cost of IVR(C) is dominated by $O(n_{1,\gamma} n_{1,D})$.

4. Dynamic flux surrogate-based partitioned methods

In this section we formulate a surrogate-based instance of the partitioned framework in Section 3, which uses data-driven techniques to construct the synchronization operators \mathcal{F}_i in (16). At the core of this construction is an accurate surrogate model for the dynamics of the interface flux. In this paper we consider surrogates having the form of a generic linear discrete time dynamical system

$$\mathbf{y}_{k+1} = A \mathbf{y}_k, \tag{24}$$

where $\mathbf{y}_k \in \mathbb{R}^{N_{\text{FS}}}$ is the state of the system at the current time t_k , \mathbf{y}_{k+1} is the predicted state at the future time step, and A is $N_{\text{FS}} \times N_{\text{FS}}$ linear dynamics operator.

Application of the flux surrogate in (24) amounts to a single matrix-vector multiplication per time step, which requires $N_{\text{FS}}(2N_{\text{FS}} - 1)$ flops. Our goal is to learn an operator A whose computational cost is comparable to that of IVR(L), but whose accuracy approaches that of IVR(C). To that end we shall apply the Dynamic Mode Decomposition (DMD) technique, reviewed in Section 2.2, to a snapshot matrix \mathbf{Y} containing solutions of the coupled problem (8)–(9). To achieve the desired computational efficiency of

⁵We recall that $n_{l,\gamma}$ is the dimension of the interface space $S_{l,\gamma}^h$ used to approximate the Lagrange multiplier.

⁶We do not include the computation of the load vectors $\mathbf{b}_{i,k}$ into the cost estimate of IVR because they have to be computed regardless of the partitioned scheme employed.

the dynamic flux surrogate, we will construct its state by taking into account the local nature of the interface flux. Meeting the accuracy goal requires accurate snapshots of the interface flux. This rules out the finite element flux $F_i(u_i^h)$ because it is only first-order accurate whenever $\kappa_i > 0$. Instead, we shall solve the coupled problem (8)–(9) by using the IVR(C) scheme and utilize the Lagrange multiplier approximations produced by this scheme to define the flux snapshots. We will first discuss construction of the DMD flux surrogate for (8)–(9) with fixed diffusion coefficients on each subdomain. Then, in Section 4.2 we will extend our surrogate to handle the parameterized transmission problem.

4.1. DMD surrogate-based partitioned method for coupled PDEs

Let $\mathbf{u}_{1,k}$, $\mathbf{u}_{2,k}$, and $\boldsymbol{\lambda}_k$; $k = 0, 1, \dots$ be the coefficient vectors of the IVR(C) solution at time t_k . There are several possible ways to specialize the generic system (24) to this type of data. Since our goal is to develop a surrogate model for the dynamics of the interface flux, the most straightforward approach is to define the state of this system to be the Lagrange multiplier from the IVR solution, i.e., to construct the snapshot matrices \mathbf{Y} and \mathbf{Y}' in (2) using $\mathbf{y}_k = \boldsymbol{\lambda}_k$. However, this choice does not allow for any information exchange between the subdomains, which runs counter to the role of the Lagrange multiplier as the “glue” that keeps the subdomain states continuous across the interface. Indeed, the “synchronization” operator resulting from the choice $\mathbf{y}_k = \boldsymbol{\lambda}_k$ would generate a dynamic boundary condition for the subdomain equations without any input from their states. As a result, the flux generated by such a surrogate can drift apart from the actual flux needed to satisfy the first coupling condition in (9).

This observation suggests that the surrogate needs to be made aware of the subdomain states so that it can generate fluxes that will keep these states continuous across γ . To that end, we consider a state \mathbf{y}_k comprising the Lagrange multiplier concatenated with the subdomain solutions on either side of the interface. Depending on the time instances at which one samples these fields, such a state can be constructed in two different ways.

Let t_k be the current time step at which we seek an estimate of the interface flux. The first way to define a state for our flux surrogate is to view the DMD operator as an explicit time integrator and sample all fields at the previous time instance t_{k-1} . This construction agrees with the traditional DMD utilization in which an initial system state \mathbf{y}_0 is specified and propagated forward in time to all future states by a repeated application of the DMD operator to \mathbf{y}_0 . A flux surrogate that adheres to this viewpoint would have to act on a state defined as $\mathbf{y}_{k-1} = (\boldsymbol{\lambda}_{k-1}, \mathbf{u}_{1,k-1}, \mathbf{u}_{2,k-1})^T$ in order to produce the flux at t_k , needed for the explicit partitioned framework in Section 3.2. However, such a state does not account for the fact that more current solution information is already available at t_k . This information can be incorporated into the dynamics of the DMD operator by defining its state as

$$\mathbf{y}_{k-1} := \begin{bmatrix} \boldsymbol{\lambda}_{k-1} \\ \mathbf{u}_{1,k} \\ \mathbf{u}_{2,k} \end{bmatrix}, \quad k = 1, 2, \dots \quad (25)$$

In so doing, the surrogate model is combining the most recent solution information computed by the subdomain equations on both sides of the interface with its previous prediction of the Lagrange multiplier. Application of the DMD approach to such “staggered” states departs from its traditional use and can be interpreted as advancing the Lagrange multiplier in time in a semi-implicit manner.

However, because the state (25) includes the complete subdomain coefficient vectors, its length is $N_{\text{FS}} = n_{l,\gamma} + n_{1,D} + n_{2,D}$. As a result, the computational cost of a surrogate acting on (25) is comparable to that of IVR(C), i.e., such a surrogate will not meet our efficiency goal. At the same time it stands to reason that since the role of the interface flux is to maintain solution continuity across γ , its dynamics should not be strongly influenced by solution values away from the interface. Thus, a more economical DMD state, meeting the efficiency goal, can be designed by including only solution coefficients that are close to the interface. To formalize this idea, consider a distance threshold $0 < \delta_i < \text{diam}(\Omega_i)$, $i = 1, 2$ and let

$$\mathbf{u}_{i,k}(\delta_i) = \{(\mathbf{u}_{i,k})_j \mid \exists \mathbf{x}_j \in \Omega_i^h \text{ s.t. } d(\mathbf{x}_j, \gamma) < \delta_i\} \in \mathbb{R}^{n_{\delta_i,D}} \quad (26)$$

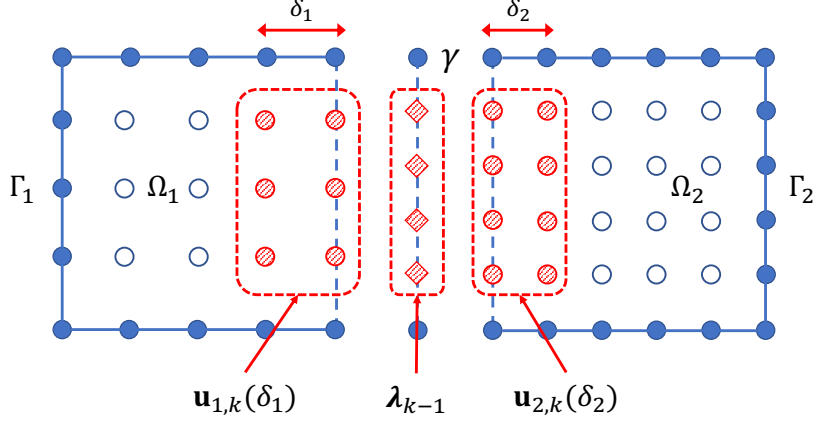


Figure 2: The staggered DMD state \mathbf{y}_{k-1} comprises interface patches $\mathbf{u}_{i,k}(\delta_i) \subset \mathbf{u}_{i,k}$ of subdomain solution coefficients at the current time t_k stacked together with the coefficient vector $\boldsymbol{\lambda}_{k-1}$ of the interface flux at the previous time t_{k-1} .

be the subset of $\mathbf{u}_{i,k}$ containing all solution coefficients located on nodes that are within distance δ_i from γ ; see Fig. 2. We shall refer to $\mathbf{u}_{i,k}(\delta_i)$ as the interface *patch* of $\mathbf{u}_{i,k}$. We now redefine the DMD state (25) by replacing the complete coefficient vectors by their interface patches as follows:

$$\mathbf{y}_{k-1} := \begin{bmatrix} \boldsymbol{\lambda}_{k-1} \\ \mathbf{u}_{1,k}(\delta_1) \\ \mathbf{u}_{2,k}(\delta_2) \end{bmatrix}, \quad k = 1, 2, \dots \quad (27)$$

The length of the redefined state is $N_{\text{FS}} = n_{l,\gamma} + n_{\delta_1,D} + n_{\delta_2,D}$. Thus, to achieve our efficiency goal we shall keep the interface patches as small as possible and roughly of the same order as the dimension of the interface space $S_{i,\gamma}^h$. In other words, we shall require $n_{\delta_i,D} = O(n_{i,\gamma})$. Section 5.4 provides further information about the selection of the interface patches.

Assume that a DMD operator A acting on the states (27) has been identified. This operator has a 3-by-3 block structure given by

$$A = \begin{bmatrix} A_{\lambda,\lambda} & A_{\lambda,u_1} & A_{\lambda,u_2} \\ A_{u_1,\lambda} & A_{u_1,u_1} & A_{u_1,u_2} \\ A_{u_2,\lambda} & A_{u_2,u_1} & A_{u_2,u_2} \end{bmatrix}$$

where the subscripts indicate the range and the domain of each block. For example, A_{λ,u_1} is a $n_{l,\gamma} \times n_{\delta_1,D}$ matrix multiplying the second sub-vector of the input state $\mathbf{y}_{k-1} = (\boldsymbol{\lambda}_{k-1}, \mathbf{u}_{1,k}(\delta_1), \mathbf{u}_{1,k}(\delta_2))^T$ and contributing to the first sub-vector of the output state $\mathbf{y}_k = (\boldsymbol{\lambda}_k, \mathbf{u}_{1,k+1}(\delta_1), \mathbf{u}_{1,k+1}(\delta_2))^T$. Since we only need predictions of the interface flux, the computational efficiency of the flux surrogate can be further improved by discarding the second and the third row in A . Thus, we define the DMD flux surrogate operator as

$$A_\lambda = [A_{\lambda,\lambda} \quad A_{\lambda,u_1} \quad A_{\lambda,u_2}].$$

In so doing, we save approximately $(N_{\text{FS}} - n_{l,\gamma})(2N_{\text{FS}} - 1)$ flops compared to the cost of the full size operator A . The truncation of the DMD operator is another key distinction between the conventional use of the DMD approach and its application as a surrogate for interface flux dynamics.

We now define the synchronization operators for the surrogate-based partitioned method as

$$\mathcal{F}_i(\boldsymbol{\lambda}_{k-1}; \mathbf{u}_{1,k}, \mathbf{u}_{2,k}) := G_i^T \boldsymbol{\lambda}_k = G_i^T A_\lambda \mathbf{y}_{k-1}, \quad (28)$$

where \mathbf{y}_{k-1} is the state defined in (27). Note that the structure of the surrogate-based synchronization operators (28) resembles that of the remap-based ones (17) in the sense that they both involve only matrix-vector multiplies and do not require any matrix inversions as in the reconstruction-based case (22). Algorithm 4 summarizes the DMD flux surrogate-based partitioned method for a set of prescribed diffusion coefficients.

Algorithm 4: DMD surrogate-based partitioned method for coupled PDEs

Offline

For $i = 1, 2$:

1. Given a diffusion coefficient κ_i , collect q equally spaced in time solution snapshots $\mathbf{u}_{1,k}$, $\mathbf{u}_{2,k}$, and $\boldsymbol{\lambda}_k$; $k = 0, \dots, q-1$ by using IVR(C) to solve (8)–(9).
2. Choose a distance threshold $0 < \delta_i < \text{diam}(\Omega_i)$ and assemble the interface patches $\mathbf{u}_{i,k}(\delta_i)$ as in (26).
3. Form the staggered states $\mathbf{y}_{k-1} = (\boldsymbol{\lambda}_{k-1}, \mathbf{u}_{1,k}(\delta_1), \mathbf{u}_{2,k}(\delta_2))^T$, the snapshot matrices \mathbf{Y} and \mathbf{Y}' , and perform Algorithm 1 to identify the *full size* DMD operator A .
4. Truncate A to obtain the DMD flux operator A_λ .

Online

Assume a partition $0 = t_0 < t_1 < \dots < t_N = T$ of the simulation time interval and compute the initial condition vectors $\mathbf{u}_{i,0}$, $i = 1, 2$. For $i = 1, 2$ and $k = 0, 1, \dots, N-1$:

1. **Synchronize:**

- 1.1 **Construct state:** Assemble \mathbf{y}_{k-1} from DMD prediction $\boldsymbol{\lambda}_{k-1}$, and subdomain patches $\mathbf{u}_{i,k}(\delta_i)$.
- 1.2 **Predict flux:** Apply A_λ to \mathbf{y}_{k-1} to obtain $\boldsymbol{\lambda}_k$ and compute $\boldsymbol{\lambda}_{i,k}^{\text{DMD}}$:

$$\boldsymbol{\lambda}_{i,k}^{\text{DMD}} = G_i^T \boldsymbol{\lambda}_k = G_i^T A_\lambda \mathbf{y}_{k-1}.$$

2. **Step in time:** Use forward Euler to solve (14) with Neumann data $\boldsymbol{\lambda}_{i,k}^{\text{DMD}}$:

$$\mathbf{u}_{i,k+1} = \mathbf{u}_{i,k} + \Delta t M_i^{-1} (\mathbf{f}_{i,k} - K_i \mathbf{u}_{i,k} + (-1)^i \boldsymbol{\lambda}_{i,k}^{\text{DMD}}).$$

4.2. DMD surrogate-based partitioned method for coupled μ PDEs

In this section we extend Algorithm 4 to handle the parameterized model transmission problem (8). To that end we shall replace the DMD flux surrogate operator in (28) by a parameterized one based on the reduced Koopman operator inference (rKOI) algorithm from Section 2.2.1. Application of rKOI requires modification of the offline phase in Algorithm 4, where now one has to sample the parameter space of the coupled μ PDE problem. Recall that (8) is parameterized by the subdomain diffusion coefficients, i.e., $\boldsymbol{\mu} = \{\kappa_1, \kappa_2\} \in \mathcal{M}$. For simplicity we consider a rectangular parameter domain defined by lower and upper bounds for each diffusion coefficient:

$$\mathcal{M} := [\kappa_{1,\min}, \kappa_{1,\max}] \times [\kappa_{2,\min}, \kappa_{2,\max}] \subset \mathbb{R}^2. \quad (29)$$

Let $\mathcal{M}_m := \{\boldsymbol{\mu}_j\}_{j=1}^m$ denote a representative set of parameter samples $\boldsymbol{\mu}_j = \{\kappa_{1,j}, \kappa_{2,j}\}$. For every parameter $\boldsymbol{\mu}_j \in \mathcal{M}_m$ we generate a set of q equally spaced in time solution snapshots $\mathbf{u}_{1,k}(\boldsymbol{\mu}_j)$, $\mathbf{u}_{2,k}(\boldsymbol{\mu}_j)$, and $\boldsymbol{\lambda}_{1,k}(\boldsymbol{\mu}_j)$; $k = 0, \dots, q-1$ by using IVR(C) to solve (8). Next, we select distance thresholds δ_i , $i = 1, 2$ and construct the corresponding interface patches. Then, we assemble the patches and the interface flux into staggered states

$$\mathbf{y}_{k-1}(\boldsymbol{\mu}_j) = (\boldsymbol{\lambda}_{1,k-1}(\boldsymbol{\mu}_j), \mathbf{u}_{1,k}(\delta_1; \boldsymbol{\mu}_j), \mathbf{u}_{2,k}(\delta_2; \boldsymbol{\mu}_j))^T$$

and use these states to precompute the full size DMD operators $\{A(\boldsymbol{\mu}_j)\}_{j=1}^m$. Truncation of these operators yields the DMD flux surrogate operator set $\{A_\lambda(\boldsymbol{\mu}_j)\}_{j=1}^m$. This completes the offline phase of the algorithm.

Algorithm 5: Surrogate-based partitioned method for coupled μ PDEs

Offline

1. Sample \mathcal{M} in a region of interest to define a parameter set \mathcal{M}_m .
2. For every $\boldsymbol{\mu}_j \in \mathcal{M}_m$ learn $A_\lambda(\boldsymbol{\mu}_j)$ by performing steps 1–4 in the offline stage of Algorithm 4.

Online

Assume a partition $0 = t_0 < t_1 < \dots < t_N = T$ of the simulation time interval and compute the initial condition vectors $\mathbf{u}_{i,0}$, $i = 1, 2$.

Compute rKOI DMD surrogate: Given $\boldsymbol{\mu} \in \mathcal{M}$ choose a ball $B(\boldsymbol{\mu}, R)$, form the set $\mathcal{M}_m(\boldsymbol{\mu}, r)$ as in (7), and set

$$A_\lambda(\boldsymbol{\mu}) := \sum_{\boldsymbol{\mu}_j \in \mathcal{M}_m(\boldsymbol{\mu}, r)} \ell_{\boldsymbol{\mu}_j}(\boldsymbol{\mu}) A_\lambda(\boldsymbol{\mu}_j) \quad (31)$$

where $\ell_{\boldsymbol{\mu}_j}$ is the Lagrange polynomial basis for the parameter set $\mathcal{M}_m(\boldsymbol{\mu}, r)$.

For $i = 1, 2$ and $k = 0, 1, \dots, N-1$

1. **Synchronize:**

- 1.1 **Construct state:** Assemble \mathbf{y}_{k-1} from DMD prediction $\boldsymbol{\lambda}_{k-1}$, and subdomain patches $\mathbf{u}_{i,k}(\delta_i)$.
- 1.2 **Predict flux:** Apply the rKOI operator $A_\lambda(\boldsymbol{\mu})$ to \mathbf{y}_{k-1} to obtain $\boldsymbol{\lambda}_k$ and compute $\boldsymbol{\lambda}_{i,k}^{\text{DMD}}$:

$$\boldsymbol{\lambda}_{i,k}^{\text{DMD}} = G_i^T \boldsymbol{\lambda}_k = G_i^T A_\lambda(\boldsymbol{\mu}) \mathbf{y}_{k-1}.$$

2. **Step in time:** Use forward Euler to solve (14) with Neumann data $\boldsymbol{\lambda}_{i,k}^{\text{DMD}}$:

$$\mathbf{u}_{i,k+1} = \mathbf{u}_{i,k} + \Delta t M_i^{-1} (\mathbf{f}_{i,k} - K_i \mathbf{u}_{i,k} + (-1)^i \boldsymbol{\lambda}_{i,k}^{\text{DMD}}).$$

During the online phase one uses the operators $\{A_\lambda(\boldsymbol{\mu}_j)\}_{j=1}^m$ to compute the rKOI operator $A_\lambda(\boldsymbol{\mu})$ for any parameter value $\boldsymbol{\mu} \in \mathcal{M}$. Thus, instead of (28), the synchronization operators are now defined as

$$\mathcal{F}_{i,\boldsymbol{\mu}}(\boldsymbol{\lambda}_{k-1}; \mathbf{u}_{1,k}, \mathbf{u}_{2,k}) := G_i^T \boldsymbol{\lambda}_k = G_i^T A_\lambda(\boldsymbol{\mu}) \mathbf{y}_{k-1}. \quad (30)$$

This completes the extension of Algorithm 4 to the parameterized case. This extended version is summarized in Algorithm 5.

5. Training of the DMD flux surrogates

In what follows we provide a concise summary of the approach used in this paper to generate training data for the DMD flux surrogates. Section 5.1 states the model problem configuration and Section 5.2 considers the case when this problem is augmented with homogenous Dirichlet boundary conditions and has no source term. Then, in Section 5.3, we consider generation of training data for general Dirichlet conditions and source terms. The construction of the interface patches is discussed in Section 5.4. We recall that in all cases the training data is obtained by using IVR(C) to solve a properly configured model problem.

5.1. Training configuration of the model problem

For simplicity we consider a computational domain Ω defined as the unit square $[0, 1] \times [0, 1]$ with $\Omega_1 = [0, 0.5] \times [0, 1]$ and $\Omega_2 = [0.5, 1] \times [0, 1]$. Thus, γ is the line $x = 0.5$; see Figure 3 (left). However,

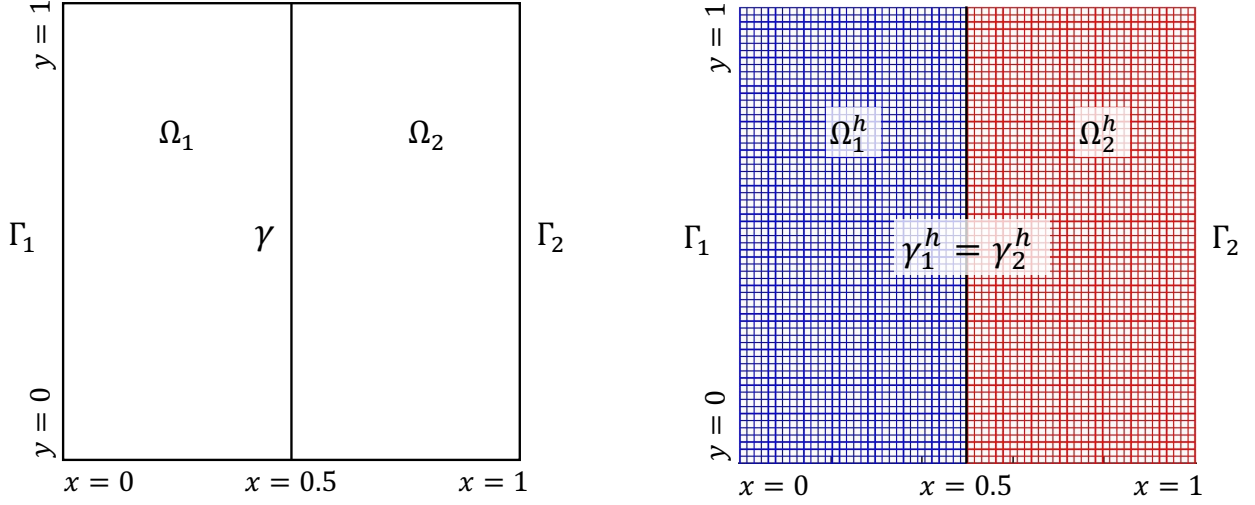


Figure 3: Typical configuration for the generation of the training data. Left: Computational domain Ω and its partition into subdomains Ω_1 and Ω_2 . Right: finite element partition Ω^h and the induced subdomain and interface grids Ω_i^h and γ_i^h ; $i = 1, 2$, respectively, for $N = 64$.

the procedure described here is applicable to general domain and interface configurations. Recall that the model transmission problem is parameterized by the diffusion coefficients, i.e., $\boldsymbol{\mu} = \{\kappa_1, \kappa_2\}$, while the source term, the boundary conditions and the advective term are assumed fixed. Here we shall define the latter using the rotating velocity field $\mathbf{v} = (0.5 - y, x - 0.5)$. We set the simulation time interval to $[0, 2\pi]$, i.e., $T = 2\pi$. Thus, given an initial condition $u_{i,0}(\mathbf{x})$, $i = 1, 2$, the solution of (8) represents one full rotation with diffusion of this initial condition. To discretize (8) in space we endow Ω with a finite element partition Ω^h comprising $N \times N$ uniform quadrilateral elements with mesh size $h = 1/N$. Restriction of Ω^h to Ω_i and γ induces subdomain meshes Ω_i^h and interface partitions γ_1^h and γ_2^h with matching grid nodes; see Figure 3 (right).

To generate the training data we solve (8), augmented with appropriate initial and boundary conditions, on this mesh using the IVR(C) scheme with a uniform time step Δt . This time step is selected to satisfy the Courant–Friedrichs–Lewy condition on Ω^h , required for the stability of the explicit Euler scheme (15) employed by IVR(C). Thus, the training data comprises time series for the subdomain solutions and the interface flux, each of length $q = 2\pi/\Delta t$. Since Δt varies with h , the length of these time series also varies with the mesh size.

5.2. Training data generation without source terms

We first consider the case when the model transmission problem is augmented with homogeneous boundary conditions and has no source terms. The “combination” test case in Section 6 is one example of this configuration. We seek to define a training set for this type of problems that will enable the inference of accurate DMD flux surrogates. In particular, given (8) with arbitrary initial conditions, the surrogate should be able to predict the interface flux with accuracy comparable to that of the IVR(C) scheme.

To define our training set we shall invoke an analogy with the identification of linear time invariant systems (LTIs), specifically the fact that an LTI system is completely characterized by its impulse response. Applying this analogy to the interface flux suggests that we can characterize its dynamics by collecting data about the spatial “impulse response” of (14) along the interface. Thus, we propose to generate the training data by computing the solution of (14) for a set of initial conditions $\{u_{i,0}^j\}_{j=1}^P$, comprising Gaussian hills with standard deviation σ and centers (x_0, y_0) , i.e., functions having the following general form:

$$\psi(x, y; x_0, y_0) = e^{-\frac{(x-x_0)^2 + (y-y_0)^2}{2\sigma^2}}. \quad (32)$$

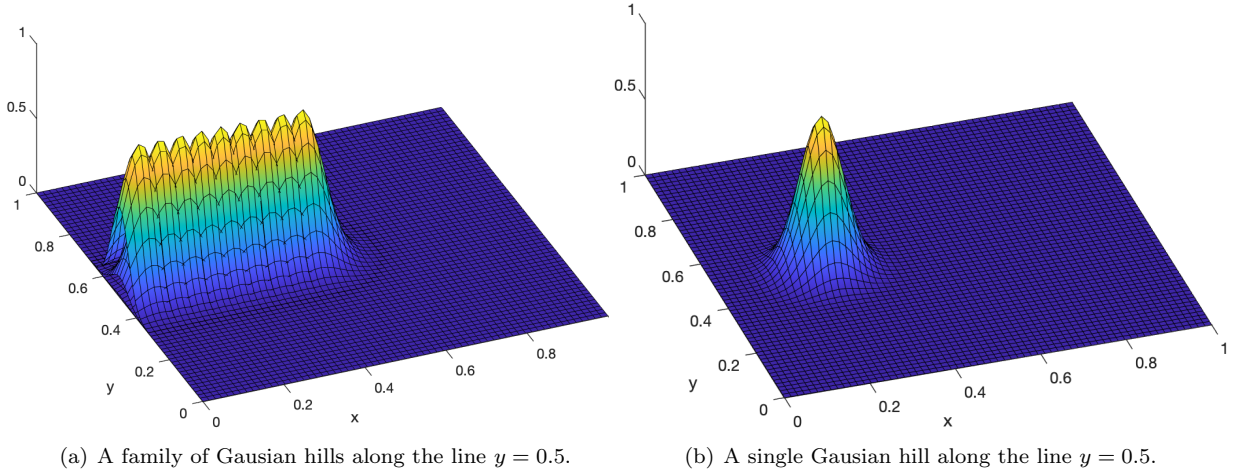


Figure 4: Typical examples of Gaussian hill initial conditions used to generate the training data for the DMD flux surrogate.

To define this set we place the centers of the Gaussian hills at uniform distances from each other along the segment $S = \{(x, y) \in \Omega_1 \mid 0 \leq x \leq 0.5 \text{ and } y = 0.5\}$. The spacing between these centers is chosen to be of the same order as the mesh size h of the finite element partition Ω^h . Likewise, we set the standard deviation for each Gaussian to be $O(h)$. As a result, these Gaussians can be thought of as smooth approximations of the Dirac’s delta function on the finite element mesh, further highlighting the parallels with an impulse response of a system.

The training data is then generated by using IVR(C) to solve (8) for each initial condition in the set $\{u_{i,0}^j\}_{j=1}^P$. The exact solutions corresponding to these initial conditions are circular paths of diffusing Gaussians about the domain center $(x, y) = (0.5, 0.5)$. With this choice of Gaussian sizes and initial spacings, the interface γ defined by $x = 0.5$ experiences crossings everywhere when the entire set of initial conditions is used. In so doing, we obtain a training set that contains detailed information about the dynamics of the interface flux along the entire interface.

5.3. Training data generation with source terms

In Section 5.2 we described generation of training data for homogeneous Dirichlet conditions and no source terms. Here we briefly discuss the general case when the model problem is augmented with inhomogeneous boundary conditions and/or source terms. Besides being of a practical importance, such a configuration arises when testing a numerical scheme for (8) using the method of manufactured solutions. In such cases it is common for a manufactured source term and boundary conditions to appear. We will need such training data to perform the “patch” test in Section 6.

It is important to keep in mind that in this paper we restrict attention to a μ PDE version of (8) parameterized solely by the diffusion coefficients. Thus, we do not consider a case where the boundary conditions and/or the source terms are also a part of the problem parameterization. Such settings are beyond the main scope of this paper, which is to demonstrate a proof-of-principle for a dynamic flux surrogate-based partitioned scheme.

The introduction of a source term changes the dynamics of the original system and thus destroys the applicability of the DMD operators created using homogeneous Dirichlet boundary conditions and no source terms in Section 5.2. In order to incorporate the effects of source term and boundary conditions into the DMD surrogate model, we must generate the Gaussian initial condition data as in Section 5.2, but with the appropriate boundary and source terms. Specifically, given a source term f_i and Dirichlet data g_i , $i = 1, 2$ we use IVR(C) to solve (8) for every initial condition in the set $\{u_{i,0}^j\}_{j=1}^P$.

5.4. Construction of the interface patches

In order to enable information exchange between the subdomains, the DMD state \mathbf{y}_k must include information from the subdomain solutions. Recall that if we define this state as in (4.1), i.e., by including the entire subdomain solution coefficient vectors, the computational cost of the DMD surrogate is comparable to that of the IVR(C) scheme and does not meet our efficiency goal. Essential to achieving this goal is the utilization of interface patches $\mathbf{u}_{i,k}(\delta_i) \subset \mathbf{u}_{i,k}$ instead of the entire coefficient vectors.

Implementation of the interface patch definition (26) on non-uniform grids can be performed by using k -rings or a $k-d$ tree search, which is generally applicable to DoFs that have a correlation to physical space, such as those in Lagrangian C^0 finite element spaces. For the unit square domain and the uniform quadrilateral grids considered in this paper, implementation of (26) is fairly straightforward and amounts to selecting all DoFs located on vertical grid lines within the prescribed distance threshold from the interface; see Figure 2.

In this case it is also convenient to measure the patch sizes by the number of grid lines included in their definition. Thus, in what follows, we shall say that $\mathbf{u}_{i,k}(\delta_i)$ is an interface patch of size K if it contains all solution coefficients located on the interface mesh γ_i^h and the $K-1$ adjacent grid lines. For example, the patches shown in Figure 2 both have size 2.

6. Numerical Results

In this section we demonstrate numerically the performance of the DMD flux surrogate-based partitioned scheme (DMD-FS) formulated in Section 4. To that end we compare and contrast the accuracy and efficiency of this scheme with the IVR(C) and IVR(L) methods using two different solutions and two distinct parameter settings for the diffusion coefficient in the model transmission problem. In all cases we use a rotating velocity field $\mathbf{v} = (0.5 - y, x - 0.5)$ to define the advective term in (8).

The first solution is given by the linear in time and piecewise linear in space function

$$u(x, y) = \begin{cases} t(x + 2y + 3) & \text{if } (x, y) \in \bar{\Omega}_1 \\ t \left(\frac{\kappa_1}{\kappa_2} x + 2y + \frac{\kappa_2 - \kappa_1}{2\kappa_2} + 3 \right) & \text{if } (x, y) \in \Omega_2 \end{cases}, \quad (33)$$

where κ_i is the diffusion coefficient on Ω_i . The coefficients on Ω_2 are defined so that the manufactured solution satisfies the coupling conditions in (9) for any combination of positive diffusion coefficients κ_i , $i = 1, 2$. Note that for $\kappa_1 \neq \kappa_2$ this solution has a “kink” along the interface that is necessary to match the fluxes on both sides of γ ; see Figure 5(a). We define source terms and boundary data matching the manufactured solution by inserting (33) into the governing equations and the boundary condition of the model problem (8), respectively. As mentioned in Section 5.3, these manufactured source terms and boundary conditions are used to generate training data that represents the dynamics of the interface flux produced by (33). We refer to this example as the “patch test” because, on meshes with matching interface nodes, both IVR(C) and a monolithic discretization of (8) will recover (33) to machine precision. While we do not expect IVR(L) and DMD-FS schemes to have this property, the patch test provides verification of the IVR(C) scheme.

The second solution is defined by homogeneous Dirichlet boundary conditions, homogeneous source terms and an initial condition considered in [53]. This initial condition comprises a Gaussian hill, cone, and slotted cylinder from [54] augmented by a “staircased” cylinder; see Figure 6. We refer to this test as the “combination test.” The combination test is designed to examine how well a scheme can handle initial condition sets with varying degrees of smoothness.

We pair both of these solutions with two different combinations of the diffusion coefficients in (8). The first one is characterized by diffusion coefficients that are discontinuous along the interface, i.e., $\kappa_1 \neq \kappa_2$. We refer to this case as the “multi-material” configuration of the model problem. The second combination uses the same diffusion coefficient in both subdomains, i.e., $\kappa_1 = \kappa_2$, and is referred to as the “single material” configuration of (8).

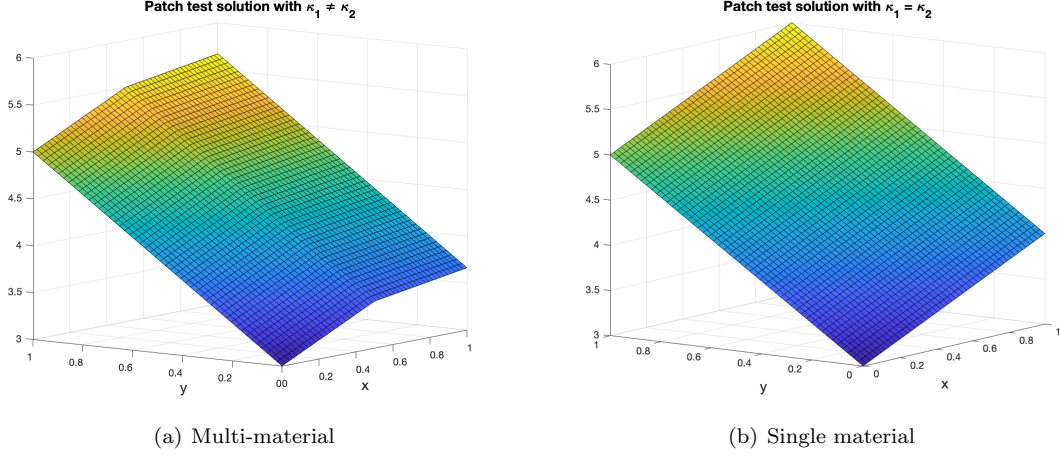


Figure 5: A multi-material patch test solution with $\kappa_1 = 1 \times 10^{-3}$, $\kappa_2 = 3 \times 10^{-3}$ and single material patch test solution with $\kappa_1 = \kappa_2 = 1 \times 10^{-3}$. Both solutions shown at $t = 1$.

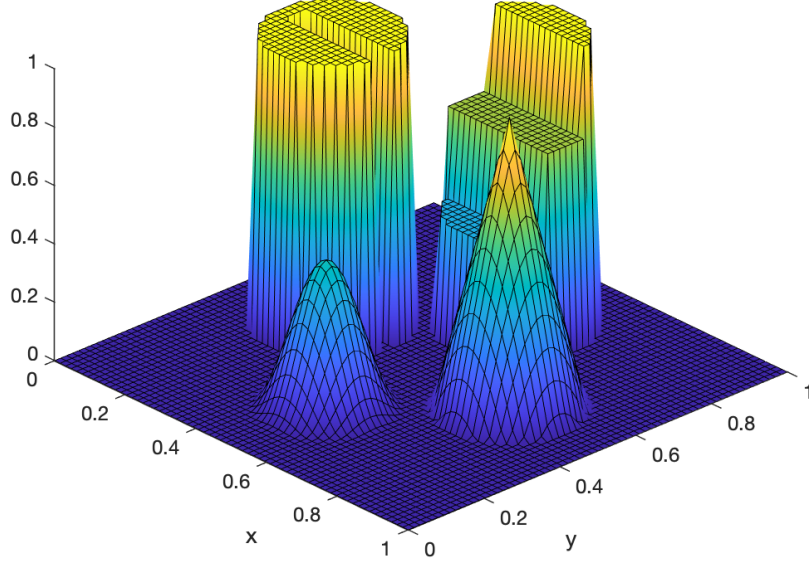


Figure 6: Initial condition for combination test.

We use the multi-material configuration of (8) to exercise the parametric version of the DMD-FS scheme defined in Algorithm 5. The single material case will be used to compare and contrast the convergence of this scheme with that of the IVR(C) and IVR(L) methods. To that end we shall use the fixed parameter version of DMD-FS given in Algorithm 4.

In all numerical studies below, we report the solution error of the IVR(C), IVR(L) and DMD-FS schemes relative to a “benchmark” solution computed by a monolithic discretization of (8) on the same mesh Ω^h that induces the subdomain and interface meshes for these schemes. The errors are measured at the final time $T = 2\pi$ after the initial condition has completed one full revolution.

Specifically, let u_M^h denote the monolithic solution of (8) on Ω_h at $T = 2\pi$ and let $u_{i,M}^h$, $i = 1, 2$ be the restrictions of this solution to Ω_i^h . Let $u_{i,C}^h$, $u_{i,L}^h$, and $u_{i,D}^h$ denote the solutions of the IVR(C), IVR(L) and DMD-FS schemes on the same mesh at the same time. For $X \in \{C, L, D\}$ we define the relative L^2 and H^1

errors of the solution $u_{i,X}^h$, $i = 1, 2$ as

$$\mathcal{E}_X^r = \frac{1}{2} \sum_{i=1}^2 \frac{\|u_{i,X}^h - u_{i,M}^h\|_{r,\Omega_i}}{\|u_{i,M}^h\|_{r,\Omega_i}}, r = 0, 1. \quad (34)$$

Since the combination test problem does not have a closed form solution, this approach ensures consistency in reporting the errors.

6.1. Multi-material Configuration

For both multi-material tests we use a uniform $N \times N$ grid with $N = 64$ and mesh size $h = 1/64$. The time step $\Delta t = 3.37E - 3$ is selected to satisfy the Courant–Friedrichs–Lewy (CFL) condition on this mesh, necessary for the stability of the explicit Euler scheme (15) in the partitioned framework. This time step results in training data comprising time series of length $q = 1866$ for the subdomain solutions and the interface flux, respectively.

Patch test. For this test we define the parameter domain as $\mathcal{M} = ([1, 2] \times [2, 3]) \times 10^{-3}$ and sample the solution at the four corners of this set, i.e., $m = 4$ and

$$\mathcal{M}_m = \{(1, 2), (1, 3), (2, 2), (2, 3)\} \times 10^{-3}.$$

Training data is generated by using IVR(C) to solve (8) for all $\boldsymbol{\mu}_j \in \mathcal{M}_m$. The manufactured source term and boundary data for each parameter $\boldsymbol{\mu}_j = (\kappa_{1,j}, \kappa_{2,j})$ are defined by inserting this parameter into the definition of the exact solution (33). Given a parameter $\boldsymbol{\mu}_j$ we construct a DMD flux surrogate $A_\lambda(\boldsymbol{\mu}_j)$ using Algorithm 1 with $\epsilon = 10^{-13}$ in the relative snapshot energy condition (5). In all cases the interface patch size is 2, which corresponds to a distance threshold $\delta_i \approx 2h$ in (26).

Multi-material Patch Test			
	\mathcal{E}_X^0	\mathcal{E}_X^1	Speedup
IVR(C)	1.18E-14	2.03E-12	N/A
IVR(L)	1.69E-4	1.94E-3	$\times 3.41$
DMD-FS	6.06E-5	3.97E-3	$\times 16.66$

Table 1: Relative L^2 and H^1 errors of the multi-material patch test solutions computed by the IVR(C), IVR(L) and DMD-FS schemes at the final time $T = 2\pi$, along with the speedup of IVR(L) and DMD-FS relative to IVR(C).

To test the parametric version of the DMD-FS scheme we choose $\boldsymbol{\mu} = (1.5, 2.5) \times 10^{-3}$ and compute the solution of (8) according to Algorithm 5. Table 1 reports the relative solution errors and the speedups, relative to IVR(C), of the IVR(L) and DMD-FS schemes observed in this test.

Combination test. For this test we consider a parameter domain $\mathcal{M} = ([1, 2] \times [3, 4]) \times 10^{-3}$. As before, to generate the training data we sample the four corners of \mathcal{M} so that $m = 4$ and

$$\mathcal{M}_m = \{(1, 3), (1, 4), (2, 3), (2, 4)\} \times 10^{-3}.$$

Likewise, training data is generated by using IVR(C) to solve (8) for all $\boldsymbol{\mu}_j \in \mathcal{M}_m$, except that now the model problem is augmented with homogeneous source term and homogeneous boundary data for all parameter values. To obtain the operators $A_\lambda(\boldsymbol{\mu}_j)$, $m = 1, \dots, 4$ we apply Algorithm 1 with the same interface patch size and tolerance as in the patch test. To test the parametric DMD-FS for this example we choose $\boldsymbol{\mu} = (1.5, 3.5) \times 10^{-3}$ and use Algorithm 5 to solve the model problem. Results from the multi-material combination test are presented in Table 2, Figures 7(a)–7(d), and Figures 8(a)–8(c).

Multi-material Combination Test			
	\mathcal{E}_X^0	\mathcal{E}_X^1	Speedup
IVR(C)	2.49E-03	7.70E-03	N/A
IVR(L)	3.61E-02	8.35E-02	$\times 1.39$
DMD-FS	2.95E-03	9.71E-03	$\times 11.63$

Table 2: Relative L^2 and H^1 errors of the multi-material combination test solutions computed by the IVR(C), IVR(L) and DMD-FS schemes at the final time $T = 2\pi$, along with average speedup of the latter two relative to IVR(C).

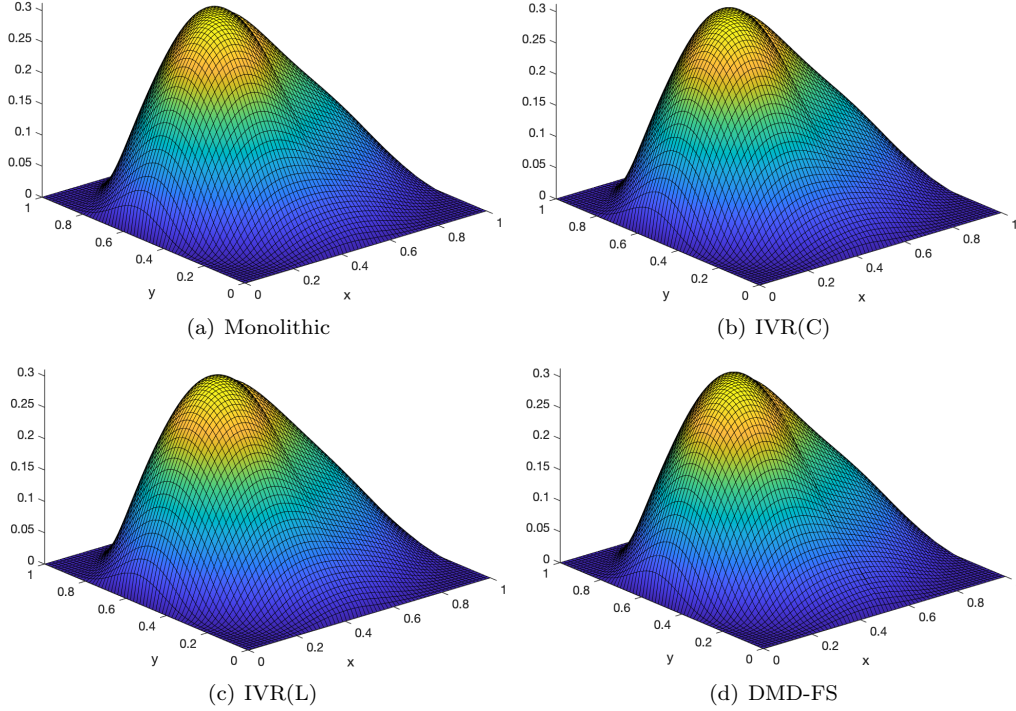
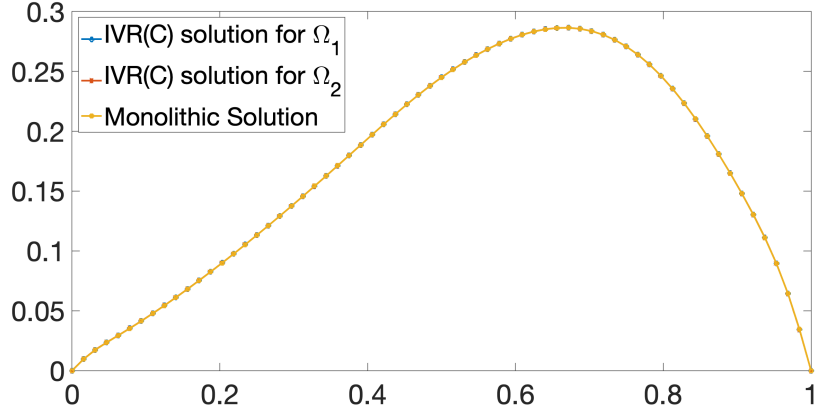


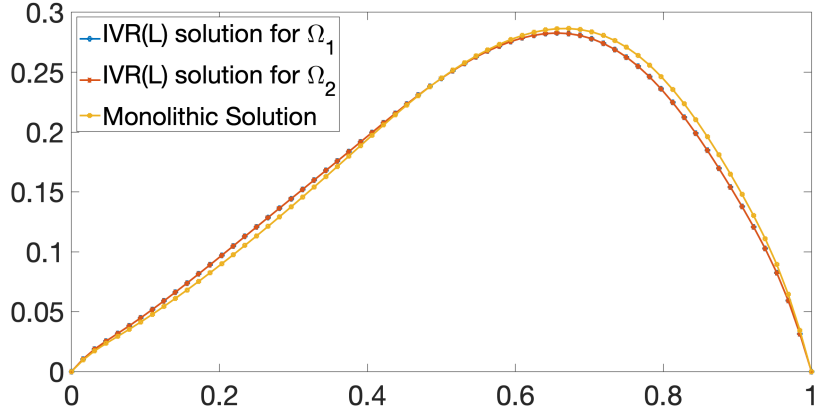
Figure 7: Surface plots of the reference monolithic solution and the solutions of the partitioned schemes for the multi-material combination test at the final simulation time $T = 2\pi$.

Discussion of results. As expected, the data in Table 1 confirms that the IVR(C) solution matches the monolithic solution of (8), and by extension - the manufactured solution (33), to machine precision. Furthermore, the relative errors reported in Tables 1–2 suggest that the DMD-FS scheme largely meets our stated accuracy goal. In particular, for the multi-material combination test the relative L^2 and H^1 errors of DMD-FS are within 1% and 26% of the IVR(C) errors, respectively. In contrast, the relative errors of IVR(L) are approximately one order of magnitude larger than those of DMD-FS. While these distinctions are hardly noticeable in the surface plots of the solutions in Figures 7(a)–7(d), they become visible when examining the profiles of the IVR(C), IVR(L) and DMD-FS solutions along the interface. From the plots in Figures 8(a)–8(c), one can clearly see that IVR(L) solution deviates the most from the benchmark monolithic solution, while the profile of the DMD-FS solution is indistinguishable from that of the IVR(C) solution.

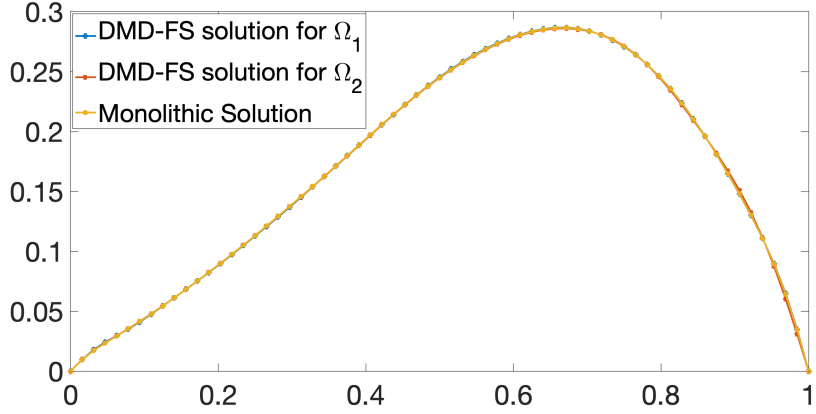
For the patch test the DMD-FS scheme meets the accuracy goal with respect to the relative L^2 error, where it outperforms the IVR(L) scheme. However, the relative H^1 error of IVR(L) is slightly better. The difference in the DMD-FS performance can be explained by observing that while the patch test has a “simpler” solution than the combination test, the latter has a simpler data structure due to the homogeneous source terms and boundary conditions. In contrast, the source terms and the boundary conditions in the patch test depend both on time and the diffusion coefficients.



(a) IVR(C)



(b) IVR(L)



(c) DMD-FS

Figure 8: Interface restrictions of the reference monolithic solution and the solutions of the partitioned schemes for the multi-material combination test at the final simulation time $T = 2\pi$.

Insofar as the computational efficiency of DMD-FS is concerned, recall that our goal was a scheme whose cost is comparable to that of the IVR(L) scheme. The data in Tables 1–2 shows that DMD-FS clearly

DMD-FS snapshot energy thresholds and ranks				
	Combination test		Patch test	
Grid	ϵ	Rank	ϵ	Rank
16×16	1E-8	29	1E-8	14
32×32	1E-8	30	1E-11	29
64×64	1E-8	42	1E-13	45
128×128	1E-9	56	1E-15	59

Table 3: Selection of the threshold ϵ for the relative snapshot energy condition (5) for each mesh size and the resulting ranks of the DMD-FS operators for the combination test and the patch test problems.

exceeds this goal for both examples. It is almost five times faster than IVR(L) for the patch test and more than eight times faster for the combination test. The speedups over IVR(C) are even more pronounced, confirming the potential of the surrogate-based approach formulated in this paper.

6.2. Single Material Configuration

For the single material configuration we use $\kappa_1 = \kappa_2 = 1 \times 10^{-3}$ for both the patch test and the combination test problems. We solve these problems using the IVR(C), IVR(L) and DMD-FS schemes on a sequence of uniform $N \times N$ quadrilateral grids with $N = 16$, $N = 32$, $N = 64$, and $N = 128$. The time steps for each grid size are selected to satisfy the CFL condition and are given by $\Delta_{16}t = 1.42 \times 10^{-2}$, $\Delta_{32}t = 6.84 \times 10^{-3}$, $\Delta_{64}t = 3.37 \times 10^{-3}$, and $\Delta_{128}t = 1.67 \times 10^{-3}$, respectively. As a result, the number of time steps required to reach the final time $T = 2\pi$ is different on every grid and is given by $q_{16} = 444$, $q_{32} = 918$, $q_{64} = 1866$, and $q_{128} = 3761$, respectively.

For every grid size N we train a separate DMD flux surrogate operator using training data specific to the grid size and the test problem. This data is generated by prescribing the initial conditions given by the Gaussian hills in Section 5.2 and then augmenting (8) with source terms and boundary conditions corresponding to the patch test and the combination test problems. Once properly configured, the model problem is solved using the IVR(C) scheme.

To account for variations in the grid size we scale the Gaussian hills in a manner proportional to the mesh size $h = 1/N$, i.e., we double the number of Gaussian hills used in training and half their width when we reduce the mesh size by half. For example, a 128×128 grid will use twice as many Gaussians for training the DMD operator as a 64×64 grid. Because the number of time steps required to reach the final time $T = 2\pi$ is different for each grid, the lengths of the time series for the subdomain solutions and the interface flux comprising the training data are also different and are given by the numbers q_N , $N \in \{16, 32, 64, 128\}$ defined earlier.

To train the DMD flux surrogate operators we apply Algorithm 1 with the relative snapshot energy threshold ϵ dependent on the test problem and/or the grid size parameter N . Table 3 shows the values of this threshold for each test problem and grid size along with the ranks of the resulting DMD flux operators. The data in this table reveals that the bulk of the snapshot energy can be captured by a relatively small number of modes, which is essential for the efficiency of the DMD operator. This observation is further confirmed by the plots of the snapshot energies in Figures 9(a)–9(b). Finally, we set the distance threshold in (26) to be $\delta_i = 5/2h$. With this choice the interface patch size remains the same on all grids and equals two.

Results for the single material configuration are collected in two tables and two figures. Table 4 shows relative solution errors and speedups for the patch test, whereas Table 5 shows this data for the combination test. For the latter we also provide surface plots of the monolithic, IVR(C), IVR(L), and DMD-FS solutions in Figures 10(a)–10(d), respectively, as well as plots of the profiles of these solutions along the interface in Figures 11(a)–11(c).

Discussion of results. Our results in the single material case largely mirror those in the multi-material setting, except that now DMD-FS consistently outperforms IVR(L) not only in terms of computational cost

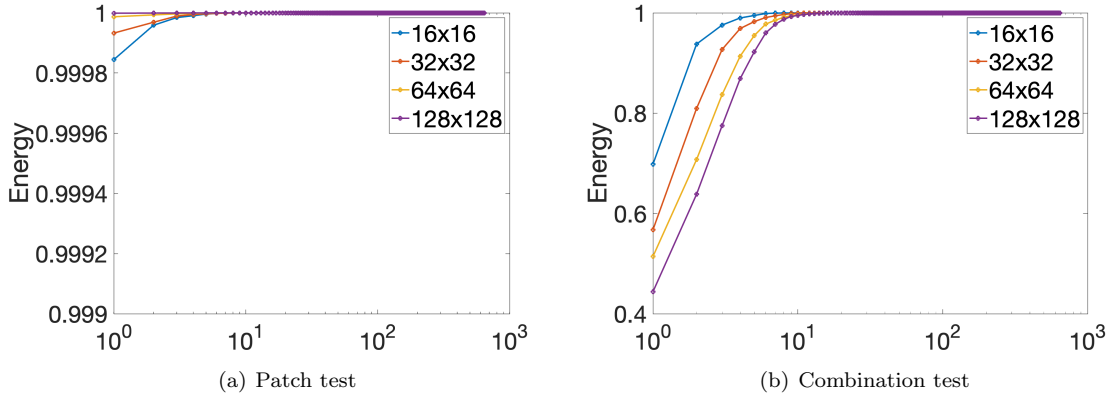


Figure 9: Snapshot energy as a function of the DMD rank for the grids used in the single material configuration.

but also in terms of accuracy. The accuracy distinction is particularly strong for the patch test where on the finest mesh the relative errors of the DMD-FS solution are four orders of magnitude better than those of the IVR(L) solution; see Table 4. Likewise, data in Table 5 shows that, for the combination test, DMD-FS also reliably delivers more accurate solutions than IVR(L) while being several times faster than the latter. Most notably, we see double digit speedups relative to IVR(C) for both test problems on all meshes, further confirming the potential of the DMD-FS approach to produce accurate solutions at a fraction of the cost of the IVR(C) scheme.

Interestingly enough, for the combination test in the single material case, the distinctions between IVR(L) and the other schemes are already perceptible in the surface solution plots shown in Figures 10(a)–10(d), which reveal the more diffusive nature of the IVR(L) scheme. The higher rate of dissipation in IVR(L) is also visible in the plots of the solution profiles along the interface in Figures 11(a)–11(c). In contrast, the profile of the DMD-FS solution is again indistinguishable from that of the IVR(C) solution.

7. Conclusion

In this paper we introduced the notion of a dynamic flux surrogate-based partitioned scheme as a way to bridge the accuracy and performance gaps between reconstruction-based and remap-based schemes. To demonstrate the potential of this approach, we formulated an instance of such a partitioned scheme by adapting the Dynamic Mode Decomposition system identification technique to obtain accurate and efficient surrogates for the dynamics of the interface flux.

We tested parametric and non-parametric versions of the resulting DMD-FS scheme using a multi-material and a single material configuration of a model transmission problem. The tests were carried out using a manufactured solution and a “combination” solution commonly used in the literature. In all cases we observed double digit speedups by the DMD-FS scheme relative to the IVR(C) scheme. Moreover, in terms of computation efficiency, DMD-FS also outperformed IVR(L) which was our efficiency target.

In terms of accuracy, DMD-FS exceeded the accuracy of IVR(L) in all but one case, where the relative H^1 error of IVR(L) was slightly better than that of the DMD-FS. These results confirm the potential of DMD-FS but also underscore the need for further investigation of its accuracy and in particular - the development of effective training strategies. These include both the generation of training data by proper sampling of the parameter space and exploration of the DMD performance as a function of the interface patch size and the number of modes retained.

Future work will focus on these and other developmental questions as well as on the extension of the surrogate-based approach to more complex partitioned settings such as multirate partitioned schemes. Such schemes exchange information over coupling windows and typically require multiple data transfers within

Single Material Patch Test			
IVR(C)			
Grid	\mathcal{E}_X^0	\mathcal{E}_X^1	Speedup
16×16	5.95E-15	2.19E-13	N/A
32×32	9.07E-15	7.51E-13	N/A
64×64	9.64E-15	1.41E-12	N/A
128×128	1.50E-14	4.84E-12	N/A
IVR(L)			
Grid	\mathcal{E}_X^0	\mathcal{E}_X^1	Speedup
16×16	1.16E-3	1.28E-2	$\times 1.30$
32×32	4.17E-4	6.49E-3	$\times 1.88$
64×64	1.49E-4	2.91E-3	$\times 3.08$
128×128	4.74E-5	1.05E-3	$\times 2.82$
DMD-FS			
Grid	\mathcal{E}_X^0	\mathcal{E}_X^1	Speedup
16×16	4.15E-5	1.22E-3	$\times 13.72$
32×32	1.04E-6	5.19E-5	$\times 21.56$
64×64	9.65E-8	8.12E-6	$\times 37.36$
128×128	4.74E-9	6.53E-7	$\times 17.58$

Table 4: Relative L^2 and H^1 errors of the single material patch test solutions computed by the IVR(C), IVR(L), and DMD-FS schemes at the final time $T = 2\pi$, along with average speedup of the latter two relative to IVR(C).

each one of these window. As a result, multirate schemes stand to gain significantly from the availability of data-driven surrogates that can perform accurate and efficient data transfers between the subdomains.

Acknowledgments

This material is based upon work supported by the U.S. Department of Energy, Office of Science, Office of Advanced Scientific Computing Research, Mathematical Multifaceted Integrated Capability Centers (MMICCs) program, under Field Work Proposal 22-025291 (Multifaceted Mathematics for Predictive Digital Twins (M2dt)), Field Work Proposals 23-020467 and 19-020315, and the Laboratory Directed Research and Development program at Sandia National Laboratories.

This article has been authored by an employee of National Technology & Engineering Solutions of Sandia, LLC under Contract No. DE-NA0003525 with the U.S. Department of Energy (DOE). The employee owns all right, title and interest in and to the article and is solely responsible for its contents. The United States Government retains and the publisher, by accepting the article for publication, acknowledges that the United States Government retains a non-exclusive, paid-up, irrevocable, world-wide license to publish or reproduce the published form of this article or allow others to do so, for United States Government purposes. The DOE will provide public access to these results of federally sponsored research in accordance with the DOE Public Access Plan <https://www.energy.gov/downloads/doe-public-access-plan>.

References

- [1] C. A. Felippa, K. Park, C. Farhat, Partitioned analysis of coupled mechanical systems, *Computer Methods in Applied Mechanics and Engineering* 190 (24) (2001) 3247–3270, *advances in Computational Methods for Fluid-Structure Interaction*. doi:[https://doi.org/10.1016/S0045-7825\(00\)00391-1](https://doi.org/10.1016/S0045-7825(00)00391-1). URL <https://www.sciencedirect.com/science/article/pii/S0045782500003911>

Single Material Combination Test			
IVR(C)			
Grid	\mathcal{E}_X^0	\mathcal{E}_X^1	Speedup
16×16	9.18E-15	4.97E-14	N/A
32×32	2.99E-14	4.05E-13	N/A
64×64	2.05E-14	5.22E-13	N/A
128×128	3.26E-14	1.83E-12	N/A
IVR(L)			
Grid	\mathcal{E}_X^0	\mathcal{E}_X^1	Speedup
16×16	3.37E-1	6.05E-1	$\times 1.23$
32×32	2.78E-1	5.60E-1	$\times 1.74$
64×64	1.69E-1	3.71E-1	$\times 3.16$
128×128	7.16E-2	1.63E-1	$\times 3.25$
DMD-FS			
Grid	\mathcal{E}_X^0	\mathcal{E}_X^1	Speedup
16×16	6.20E-2	1.42E-1	$\times 11.48$
32×32	2.62E-3	6.54E-3	$\times 19.63$
64×64	6.82E-4	1.69E-3	$\times 39.56$
128×128	1.25E-3	2.46E-3	$\times 26.60$

Table 5: Relative L^2 and H^1 errors of the single material combination test solutions computed by the IVR(C), IVR(L), and DMD-FS schemes at the final time $T = 2\pi$, along with average speedup of the latter two relative to IVR(C).

- [2] Y. Bazilevs, K. Kamran, G. Moutsanidis, D. J. Benson, E. Oñate, A new formulation for air-blast fluid–structure interaction using an immersed approach. part i: basic methodology and fem-based simulations, *Computational Mechanics* 60 (1) (2017) 83–100. doi:10.1007/s00466-017-1394-3.
URL <https://doi.org/10.1007/s00466-017-1394-3>
- [3] C. Newman, D. A. Knoll, Physics-based preconditioners for ocean simulation, *SIAM Journal on Scientific Computing* 35 (5) (2013) S445–S464. arXiv:<https://doi.org/10.1137/120881397>, doi:10.1137/120881397.
URL <https://doi.org/10.1137/120881397>
- [4] D. Knoll, D. Keyes, Jacobian-free newton–krylov methods: a survey of approaches and applications, *Journal of Computational Physics* 193 (2) (2004) 357–397. doi:<https://doi.org/10.1016/j.jcp.2003.08.010>.
URL <https://www.sciencedirect.com/science/article/pii/S0021999103004340>
- [5] J. M. Connors, K. C. Sockwell, A multirate discontinuous-Galerkin-in-time framework for interface-coupled problems, *SIAM Journal on Numerical Analysis* 60 (5) (2022) 2373–2404. arXiv:<https://doi.org/10.1137/21M1461149>, doi:10.1137/21M1461149.
URL <https://doi.org/10.1137/21M1461149>
- [6] X. Jiao, M. T. Heath, Common-refinement-based data transfer between non-matching meshes in multiphysics simulations, *International Journal for Numerical Methods in Engineering* 61 (14) (2004) 2402–2427. doi:10.1002/nme.1147.
URL <http://dx.doi.org/10.1002/nme.1147>
- [7] P. A. Ullrich, M. A. Taylor, Arbitrary-order conservative and consistent remapping and a theory of linear maps: Part i., *Mon. Weather Rev.* 143 (2015.) 2419–2440,.
- [8] B. Gatzhammer, Efficient and flexible partitioned simulation of fluid-structure interactions, Doctoral thesis, Technische Universitaet Muenchen, Fakultae fuer Informatik. Informatik 5 – Lehrstuhl fuer Wissenschaftliches Rechnen (September 2014).
- [9] S. R. Slaterry, Mesh-free data transfer algorithms for partitioned multiphysics problems: Conservation, accuracy, and parallelism, *Journal of Computational Physics* 307 (2016) 164 – 188. doi:<http://dx.doi.org/10.1016/j.jcp.2015.11.055>.
URL <http://www.sciencedirect.com/science/article/pii/S0021999115008037>
- [10] H.-J. Bungartz, F. Lindner, B. Gatzhammer, M. Mehl, K. Scheufele, A. Shukaev, B. Uekermann, preCICE – a fully parallel library for multi-physics surface coupling, *Computers & Fluids* 141 (2016) 250 – 258, advances in Fluid-Structure Interaction. doi:<https://doi.org/10.1016/j.compfluid.2016.04.003>.
URL <http://www.sciencedirect.com/science/article/pii/S0045793016300974>
- [11] P. Kuberry, P. Bosler, N. Trask, Compadre toolkit (Feb. 2019). doi:10.5281/zenodo.2560287.

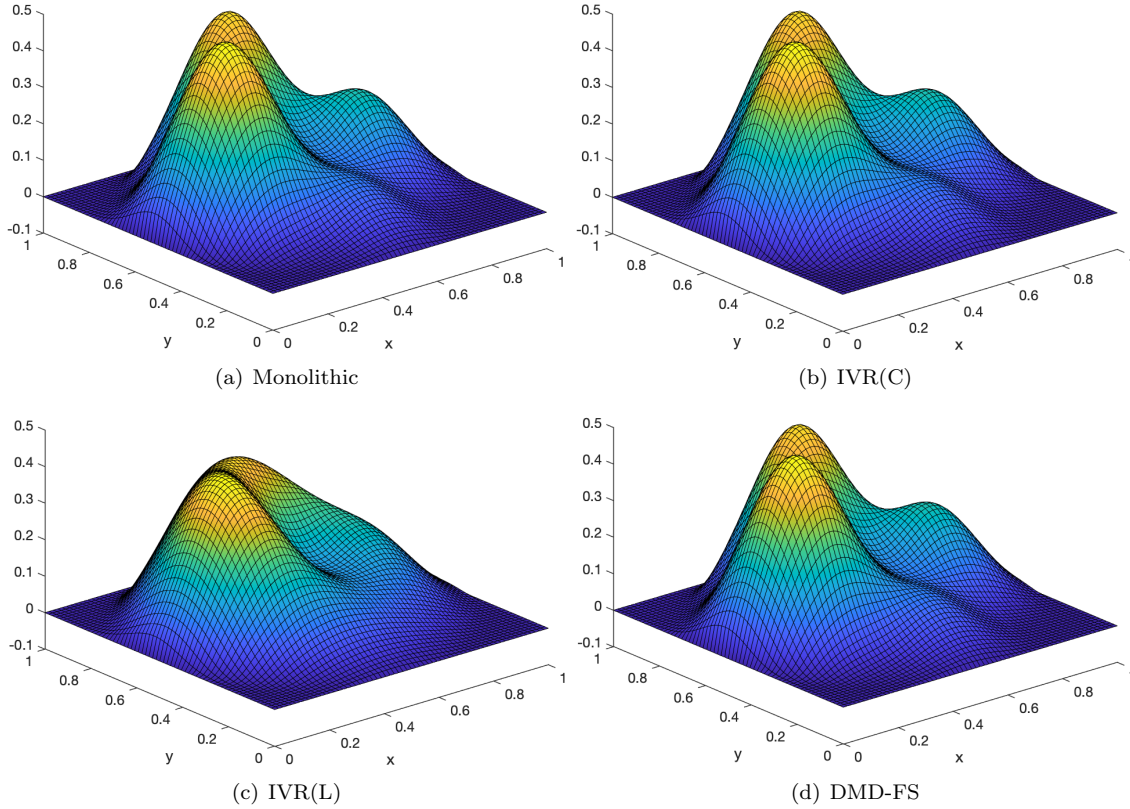
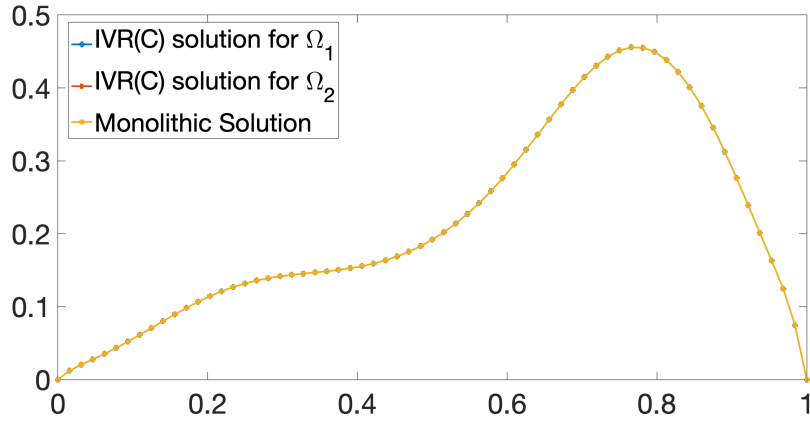
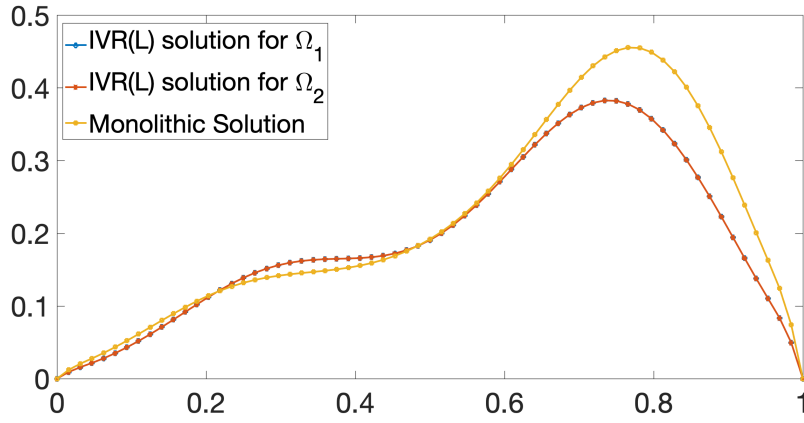


Figure 10: Surface plots of the reference monolithic solution and the solutions of the partitioned schemes for the single material combination test at the final simulation time $T = 2\pi$.

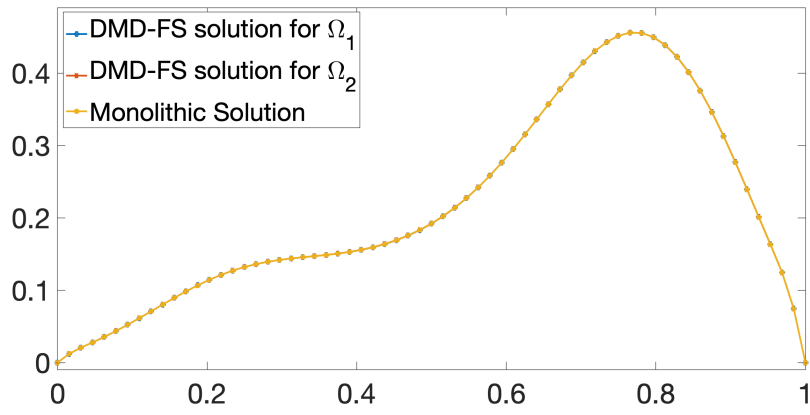
- URL <https://doi.org/10.5281/zenodo.2560287>
- [12] V. S. Mahadevan, J. E. Guerra, X. Jiao, P. Kuberly, Y. Li, P. Ullrich, R. Jacob, P. Bochev, P. Jones, Metrics for inter-comparison of remapping algorithms (mira) applied to earth system models, *Geoscientific Model Development Discussions* 2021 (2021) 1–54. doi:10.5194/gmd-2021-323.
URL <https://gmd.copernicus.org/preprints/gmd-2021-323/>
- [13] N. Collins, G. Theurich, C. DeLuca, M. Suarez, A. Trayanov, V. Balaji, P. Li, W. Yang, C. Hill, A. da Silva, Design and implementation of components in the earth system modeling framework, *International Journal of High Performance Computing Applications* 19 (3) (Fall 2005) 341–350. arXiv:<http://hpc.sagepub.com/content/19/3/341.full.pdf+html>, doi:10.1177/1094342005056120.
URL <http://hpc.sagepub.com/content/19/3/341.abstract>
- [14] P. M. Caldwell, A. Mametjanov, Q. Tang, L. P. Van Roekel, J.-C. Golaz, W. Lin, D. C. Bader, N. D. Keen, Y. Feng, R. Jacob, M. E. Maltrud, A. F. Roberts, M. A. Taylor, M. Veneziani, H. Wang, J. D. Wolfe, K. Balaguru, P. Cameron-Smith, L. Dong, S. A. Klein, L. R. Leung, H.-Y. Li, Q. Li, X. Liu, R. B. Neale, M. Pinheiro, Y. Qian, P. A. Ullrich, S. Xie, Y. Yang, Y. Zhang, K. Zhang, T. Zhou, The DOE E3SM coupled model version 1: Description and results at high resolution, *Journal of Advances in Modeling Earth Systems* n/a (n/a). arXiv:<https://agupubs.onlinelibrary.wiley.com/doi/pdf/10.1029/2019MS001870>, doi:10.1029/2019MS001870.
URL <https://agupubs.onlinelibrary.wiley.com/doi/abs/10.1029/2019MS001870>
- [15] D. Kothe, R. Szilard, P. Turinsky, CASL: The Consortium for Advanced Simulation of Light Water Reactors, Technical Report (2010).
- [16] R. Pawlowski, R. Bartlett, N. Belcourt, R. Hooper, R. Schmidt, Theory manual for multi-physics code coupling in LIME. Version 1.0, Technical Report SAND2011, Sandia National Laboratories, Albuquerque, New Mexico 87185 (March 2011).
- [17] A. P. Craig, M. Vertenstein, R. Jacob, A new flexible coupler for earth system modeling developed for CCSM4 and CESM1, *The International Journal of High Performance Computing Applications* 26 (1) (2012) 31–42. arXiv:<https://doi.org/10.1177/1094342011428141>, doi:10.1177/1094342011428141.
URL <https://doi.org/10.1177/1094342011428141>
- [18] M. Dryja, O. B. Widlund, Schwarz methods of Neumann-Neumann type for three-dimensional elliptic finite element



(a) IVR(C)



(b) IVR(L)



(c) DMD-FS

Figure 11: Interface restrictions of the reference monolithic solution and the solutions of the partitioned schemes for the single material combination test at the final simulation time $T = 2\pi$.

problems, Communications on Pure and Applied Mathematics 48 (2) (1995) 121–155. doi:10.1002/cpa.3160480203.

URL <http://dx.doi.org/10.1002/cpa.3160480203>

[19] A. Mota, I. Tezaur, G. Philpot, The Schwarz alternating method for dynamic solid mechanics, Int. J. Numer. Meth. Engng

- (2022) 1–36.
- [20] L. Gerardo-Giorda, F. Nobile, C. Vergara, Analysis and optimization of robin–robin partitioned procedures in fluid–structure interaction problems, *SIAM Journal on Numerical Analysis* 48 (6) (2010) 2091–2116. [arXiv:https://arxiv.org/abs/10.1137/09076605X](https://arxiv.org/abs/10.1137/09076605X), doi:10.1137/09076605X. URL <http://dx.doi.org/10.1137/09076605X>
 - [21] C. Förster, W. A. Wall, E. Ramm, Artificial added mass instabilities in sequential staggered coupling of nonlinear structures and incompressible viscous flows, *Computer Methods in Applied Mechanics and Engineering* 196 (7) (2007) 1278 – 1293. doi:<http://dx.doi.org/10.1016/j.cma.2006.09.002>. URL <http://www.sciencedirect.com/science/article/pii/S0045782506002544>
 - [22] A. Toth, C. T. Kelley, Convergence analysis for Anderson Acceleration, *SIAM Journal on Numerical Analysis* 53 (2) (2015) 805–819. [arXiv:https://arxiv.org/abs/10.1137/130919398](https://arxiv.org/abs/10.1137/130919398), doi:10.1137/130919398. URL <http://dx.doi.org/10.1137/130919398>
 - [23] J. Banks, W. Henshaw, D. Schwendeman, An analysis of a new stable partitioned algorithm for FSI problems. part ii: Incompressible flow and structural shells, *Journal of Computational Physics* 268 (0) (2014) 399 – 416. doi:<http://dx.doi.org/10.1016/j.jcp.2014.03.004>. URL <http://www.sciencedirect.com/science/article/pii/S0021999114001764>
 - [24] J. Banks, W. Henshaw, B. Sjögreen, A stable FSI algorithm for light rigid bodies in compressible flow, *Journal of Computational Physics* 245 (0) (2013) 399 – 430. doi:<http://dx.doi.org/10.1016/j.jcp.2013.02.050>. URL <http://www.sciencedirect.com/science/article/pii/S002199911300185X>
 - [25] M. J. Gander, Optimized schwarz methods, *SIAM Journal on Numerical Analysis* 44 (2) (2006) 699–731. [arXiv:https://arxiv.org/abs/10.1137/S0036142903425409](https://arxiv.org/abs/10.1137/S0036142903425409), doi:10.1137/S0036142903425409. URL <http://dx.doi.org/10.1137/S0036142903425409>
 - [26] M. J. Gander, Y. Xu, Optimized schwarz methods for circular domain decompositions with overlap, *SIAM Journal on Numerical Analysis* 52 (4) (2014) 1981–2004. [arXiv:https://arxiv.org/abs/10.1137/130946125](https://arxiv.org/abs/10.1137/130946125), doi:10.1137/130946125. URL <http://dx.doi.org/10.1137/130946125>
 - [27] F. LEMARIE, L. DEBREU, E. BLAYO, Toward an optimized global-in-time Schwarz algorithm for diffusion equations with discontinuous and spatially variable coefficients. part 1: The constant coefficients case, *ETNA* 40 (2013) 148–169.
 - [28] G. Carey, S. Chow, M. Seager, Approximate boundary-flux calculations, *Computer Methods in Applied Mechanics and Engineering* 50 (2) (1985) 107 – 120. doi:[http://dx.doi.org/10.1016/0045-7825\(85\)90085-4](http://dx.doi.org/10.1016/0045-7825(85)90085-4). URL <http://www.sciencedirect.com/science/article/pii/0045782585900854>
 - [29] C. Farhat, L. Crivelli, F.-X. Roux, A transient FETI methodology for large-scale parallel implicit computations in structural mechanics, *International Journal for Numerical Methods in Engineering* 37 (11) (1994) 1945–1975. doi:10.1002/nme.1620371111. URL <http://dx.doi.org/10.1002/nme.1620371111>
 - [30] K. C. Park, C. A. Felippa, R. Ohayon, Partitioned formulation of internal fluid–structure interaction problems by localized Lagrange multipliers, *Computer Methods in Applied Mechanics and Engineering* 190 (24) (2001) 2989–3007. doi:[https://doi.org/10.1016/S0045-7825\(00\)00378-9](https://doi.org/10.1016/S0045-7825(00)00378-9). URL <http://www.sciencedirect.com/science/article/pii/S0045782500003789>
 - [31] M. R. Ross, M. A. Sprague, C. A. Felippa, K. Park, Treatment of acoustic fluid–structure interaction by localized Lagrange multipliers and comparison to alternative interface-coupling methods, *Computer Methods in Applied Mechanics and Engineering* 198 (9–12) (2009) 986 – 1005. doi:<http://dx.doi.org/10.1016/j.cma.2008.11.006>. URL <http://www.sciencedirect.com/science/article/pii/S0045782508004076>
 - [32] M. R. Ross, C. A. Felippa, K. Park, M. A. Sprague, Treatment of acoustic fluid–structure interaction by localized Lagrange multipliers: Formulation, *Computer Methods in Applied Mechanics and Engineering* 197 (33–40) (2008) 3057 – 3079. doi:<http://dx.doi.org/10.1016/j.cma.2008.02.017>. URL <http://www.sciencedirect.com/science/article/pii/S0045782508000625>
 - [33] J. A. González, K. Park, Three-field partitioned analysis of fluid–structure interaction problems with a consistent interface model, *Computer Methods in Applied Mechanics and Engineering* 414 (2023) 116134. doi:<https://doi.org/10.1016/j.cma.2023.116134>. URL <https://www.sciencedirect.com/science/article/pii/S004578252300258X>
 - [34] K. C. Park, J. A. González, Y. H. Park, S. J. Shin, J. G. Kim, K. K. Maute, C. Farhat, C. A. Felippa, Displacement-based partitioned equations of motion for structures: Formulation and proof-of-concept applications, *International Journal for Numerical Methods in Engineering* n/a (n/a). [arXiv:https://onlinelibrary.wiley.com/doi/pdf/10.1002/nme.7334](https://onlinelibrary.wiley.com/doi/pdf/10.1002/nme.7334), doi:<https://doi.org/10.1002/nme.7334>. URL <https://onlinelibrary.wiley.com/doi/abs/10.1002/nme.7334>
 - [35] K. Peterson, P. Bochev, P. Kuberry, Explicit synchronous partitioned algorithms for interface problems based on lagrange multipliers, *Computers & Mathematics with Applications* 78 (2) (2019) 459–482, proceedings of the Eight International Conference on Numerical Methods for Multi-Material Fluid Flows (MULTIMAT 2017). doi:<https://doi.org/10.1016/j.camwa.2018.09.045>. URL <https://www.sciencedirect.com/science/article/pii/S0898122118305637>
 - [36] K. C. Sockwell, K. Peterson, P. Kuberry, P. Bochev, N. Trask, Interface flux recovery coupling method for the ocean–atmosphere system, *Results in Applied Mathematics* 8 (2020) 100110. doi:<https://doi.org/10.1016/j.rinam.2020.100110>. URL <http://www.sciencedirect.com/science/article/pii/S2590037420300200>
 - [37] A. Gravouil, A. Combescure, M. Brun, Heterogeneous asynchronous time integrators for computational structural dynam-

- ics, *International Journal for Numerical Methods in Engineering* 102 (3-4) (2014) 202–232. [arXiv:https://onlinelibrary.wiley.com/doi/pdf/10.1002/nme.4818](https://onlinelibrary.wiley.com/doi/pdf/10.1002/nme.4818), doi:10.1002/nme.4818.
URL <https://onlinelibrary.wiley.com/doi/abs/10.1002/nme.4818>
- [38] F. Fekak, M. Brun, A. Gravouil, B. Depale, A new heterogeneous asynchronous explicit–implicit time integrator for nonsmooth dynamics, *Comput. Mech.* 60 (1) (2017) 1–21. doi:<https://doi.org/10.1007/s0046>.
- [39] K. C. Sockwell, P. Bochev, K. Peterson, P. Kubby, Interface flux recovery framework for constructing partitioned heterogeneous time-integration methods, *Numerical Methods for Partial Differential Equations* 39 (5) (2023) 3572–3593. [arXiv:https://onlinelibrary.wiley.com/doi/pdf/10.1002/num.23015](https://onlinelibrary.wiley.com/doi/pdf/10.1002/num.23015), doi:<https://doi.org/10.1002/num.23015>.
URL <https://onlinelibrary.wiley.com/doi/abs/10.1002/num.23015>
- [40] F. Brezzi, L. D. Marini, The three-field formulation for elasticity problems, *GAMM-Mitteilungen* 28 (2) (2005) 124–153. doi:10.1002/gamm.201490016.
URL <http://dx.doi.org/10.1002/gamm.201490016>
- [41] F. Lemarié, E. Blayo, L. Debreu, Analysis of ocean-atmosphere coupling algorithms: Consistency and stability, *Procedia Computer Science* 51 (2015) 2066 – 2075, international Conference On Computational Science, {ICCS} 2015 Computational Science at the Gates of Nature. doi:<http://dx.doi.org/10.1016/j.procs.2015.05.473>.
URL <http://www.sciencedirect.com/science/article/pii/S1877050915012818>
- [42] I. Mezić, Spectral properties of dynamical systems, model reduction and decompositions, *Nonlinear Dynamics* 41 (1) (2005) 309–325. doi:10.1007/s11071-005-2824-x.
URL <https://doi.org/10.1007/s11071-005-2824-x>
- [43] C. W. Rowley, I. Mezić, S. Bagheri, P. Schlatter, D. S. Henningson, Spectral analysis of nonlinear flows, *Journal of Fluid Mechanics* 641 (2009) 115–127. doi:10.1017/S0022112009992059.
- [44] M. Aletti, D. Lombardi, A reduced-order representation of the poincaré-steklov operator: an application to coupled multi-physics problems, *International Journal for Numerical Methods in Engineering* 111 (6) (2017) 581–600. [arXiv:https://onlinelibrary.wiley.com/doi/pdf/10.1002/nme.5490](https://onlinelibrary.wiley.com/doi/pdf/10.1002/nme.5490), doi:<https://doi.org/10.1002/nme.5490>.
URL <https://onlinelibrary.wiley.com/doi/abs/10.1002/nme.5490>
- [45] S. Chen, Z. Ding, Q. Li, S. J. Wright, A reduced order schwarz method for nonlinear multiscale elliptic equations based on two-layer neural networks (2022). [arXiv:2111.02280](https://arxiv.org/abs/2111.02280).
- [46] N. Discacciati, J. S. Hesthaven, Model reduction of coupled systems based on non-intrusive approximations of the boundary response maps, *Tech. rep.*, Institute of Mathematics École Polytechnique Fédérale de Lausanne (EPFL) CH-1015 Lausanne, Switzerland (2023).
- [47] Q. A. Huhn, M. E. Tano, J. C. Ragusa, Y. Choi, Parametric dynamic mode decomposition for reduced order modeling, *Journal of Computational Physics* 475 (2023) 111852. doi:<https://doi.org/10.1016/j.jcp.2022.111852>.
URL <https://www.sciencedirect.com/science/article/pii/S0021999122009159>
- [48] P. Ciarlet, *The Finite Element Method for Elliptic Problems*, SIAM Classics in Applied Mathematics, SIAM, Philadelphia, 2002.
- [49] T. Sayadi, P. J. Schmid, F. Richecoeur, D. Durox, Parametrized data-driven decomposition for bifurcation analysis, with application to thermo-acoustically unstable systems, *Physics of Fluids* 27 (3) (2015) 037102. [arXiv:https://pubs.aip.org/aip/pof/article-pdf/doi/10.1063/1.4913868/15922234/037102_1_online.pdf](https://pubs.aip.org/aip/pof/article-pdf/doi/10.1063/1.4913868/15922234/037102_1_online.pdf), doi:10.1063/1.4913868.
URL <https://doi.org/10.1063/1.4913868>
- [50] C. Japhet, Y. Maday, F. Nataf, Robin schwarz algorithm for the nicem method: The \mathbf{P}_q finite element case, *SIAM Journal on Numerical Analysis* 52 (4) (2014) 1497–1524. [arXiv:http://dx.doi.org/10.1137/130912621](https://arxiv.org/abs/1309.12621), doi:10.1137/130912621.
URL <http://dx.doi.org/10.1137/130912621>
- [51] S. Badia, F. Nobile, C. Vergara, Fluid–structure partitioned procedures based on robin transmission conditions, *Journal of Computational Physics* 227 (14) (2008) 7027 – 7051. doi:<https://doi.org/10.1016/j.jcp.2008.04.006>.
URL <http://www.sciencedirect.com/science/article/pii/S0021999108002192>
- [52] C. Farhat, M. Lesoinne, P. L. Tallec, Load and motion transfer algorithms for fluid/structure interaction problems with non-matching discrete interfaces: Momentum and energy conservation, optimal discretization and application to aeroelasticity, *Computer Methods in Applied Mechanics and Engineering* 157 (1–2) (1998) 95 – 114. doi:[http://dx.doi.org/10.1016/S0045-7825\(97\)00216-8](http://dx.doi.org/10.1016/S0045-7825(97)00216-8).
URL <http://www.sciencedirect.com/science/article/pii/S0045782597002168>
- [53] P. Bochev, D. Ridzal, M. D’Elia, M. Perego, K. Peterson, Optimization-based, property-preserving finite element methods for scalar advection equations and their connection to algebraic flux correction, *Computer Methods in Applied Mechanics and Engineering* 367 (2020) 112982. doi:<https://doi.org/10.1016/j.cma.2020.112982>.
URL <https://www.sciencedirect.com/science/article/pii/S0045782520301651>
- [54] R. J. LeVeque, High-resolution conservative algorithms for advection in incompressible flow, *SIAM Journal on Numerical Analysis* 33 (2) (1996) 627–665. [arXiv:https://doi.org/10.1137/0733033](https://arxiv.org/abs/https://doi.org/10.1137/0733033), doi:10.1137/0733033.
URL <https://doi.org/10.1137/0733033>